Continental lithospheric temperatures: a review

Saskia Goes[1], Derrick Hasterok[2], Derek L Schutt[3], Marthe Klöcking[4]

[1] *Department of Earth Science and Engineering, Imperial College London, UK*
[2] *Department of Earth Sciences and South Australian Centre for Geothermal Research (SACGER), University of Adelaide, Australia*
[3] *Department of Geosciences, Colorado State University, Colorado, USA*
[4] *Research School of Earth Sciences, The Australian National University, Canberra, Australia*

Preprint May 2020.
Final version published in Physics of the Earth and Planetary Interiors,
Special issue on Lithosphere-Asthenosphere
doi: 10.106/j.pepi.2020.106509

Abstract

Thermal structure of the lithosphere exerts a primary control on its strength and density and thereby its dynamic evolution as the outer thermal and mechanic boundary layer of the convecting mantle. This contribution focuses on continental lithosphere. We review constraints on thermal conductivity and heat production, geophysical and geochemical/petrological constraints on thermal structure of the continental lithosphere, as well as steady-state and non-steady state 1D thermal models and their applicability. Commonly used geotherm families that assume that crustal heat production contributes an approximately constant fraction of 25-40% to surface heat flow reproduce the global spread of temperatures and thermal thicknesses of the lithosphere below continents. However, we find that global variations in seismic thickness of continental lithosphere and seismically estimated variations in Moho temperature below the US are more compatible with models where upper crustal heat production is 2-3 times higher than lower crustal heat production (consistent with rock estimates) and the contribution of effective crustal heat production to thermal structure (i.e. estimated by describing thermal structure with steady-state geotherms) varies systematically from 40-60% in tectonically stable low surface heat flow regions to 20% or lower in higher heat flow tectonically active regions. The low effective heat production in tectonically active regions is likely partly the expression of a non-steady thermal state and advective heat transport.

Keywords: continental geotherms, thermal lithosphere, heatflow, heat production, thermal conductivity

1. Introduction

The thermal structure of the lithosphere is often considered quite well understood. Half-space and plate cooling models for oceanic lithosphere [*Parsons and Sclater*,

1977] and coupled heat-flow heat-production steady-state models for continental lithosphere [*Pollack and Chapman*, 1977] developed in the 1970s are still widely used and can explain a wide range of observations (e.g., **Fig. 1)**. In the oceans, such models explain oceanic bathymetry, surface heat flow and the geoid as a function of plate age at least to good first-order [*Parsons and Sclater*, 1977; *Hillier and Watts*, 2005; *McKenzie et al.*, 2005; *Korenaga and Korenaga*, 2008; *Hasterok*, 2013]. Also bulk seismic structure of the oceanic lithosphere broadly follows an age trend suggestive of conductive cooling [*Nishimura and Forsyth*, 1989; *Ritzwoller et al.*, 2004; *Maggi et al.*, 2006; *Beghein et al.*, 2019]. In the continents, an overall correlation between tectonic age and surface heat flow has been explained with coupled heat flow-heat production models [*Pollack and Chapman*, 1977; *Chapman*, 1986; *Artemieva and Mooney*, 2001; *Hasterok and Chapman*, 2011]. The range of temperatures predicted by such models is broadly consistent with the range of seismic velocities imaged in continental lithosphere [*Röhm et al.*, 2000; *Goes and Van der Lee*, 2002; *Shapiro and Ritzwoller*, 2004a; *Priestley and McKenzie*, 2006] and variations in residual continental topography, corrected for isostatic effects of crustal density [*Hasterok and Chapman*, 2011; *Hasterok and Gard*, 2016]. In addition, such continental geotherms can be reconciled with xenolith geothermobarometry [*Rudnick et al.*, 1998; *O'Reilly and Griffin*, 2006].

However, a number of open questions remain. In the oceans, there is an unsettled debate about pure half-space cooling versus a mechanism that limits plate thickening beyond ages of about 70 Myr, such as small-scale convection and/or plume heating [*Smith and Sandwell*, 1997; *Ritzwoller et al.*, 2004; *McKenzie et al.*, 2005; *Maggi et al.*, 2006; *Afonso et al.*, 2007; *Korenaga and Korenaga*, 2008; *Zlotnik et al.*, 2008; *Adam and Vidal*, 2010; *Goutorbe*, 2010; *Hasterok*, 2013]. In addition, there may be large-scale temperature differences in the asthenosphere between the Pacific and Atlantic and/or smaller scale variations, for example, those associated with plumes or small-scale convection [*Ritzwoller et al.*, 2004; *Hillier and Watts*, 2005; *Goes et al.*, 2013]. In the continents, heat production and heat flow do not actually correlate when this is analysed carefully [*Jaupart and Mareschal*, 2007; *Hasterok and Chapman*, 2011; *Jaupart and Mareschal*, 2014; *Hasterok and Gard*, 2016], apart from in a broad sense with three classes of tectonic ages (Phanerozoic, Paleozoic, Archean) [*Pollack et al.*, 1993; *Artemieva and Mooney*, 2001]. This weak correlation leaves open the question of how variable thermal structure within and between different tectonic provinces is, to what extent these variations are controlled by variations in crustal heat production or by variations in lithospheric mantle thickness, and how significantly they deviate from a steady state thermal structure.

In this paper and another contribution in this issue [*Richards et al.*, 2020], we review the geodynamic, surface and petrological constraints on thermal structure of the continental and oceanic lithosphere, respectively. In the following, we discuss commonly used thermal models for the continental lithosphere and the observations they are based on as well as how new observations and techniques are leading to revised thermal models and new insights into how the thermal structure of continental lithosphere evolved.

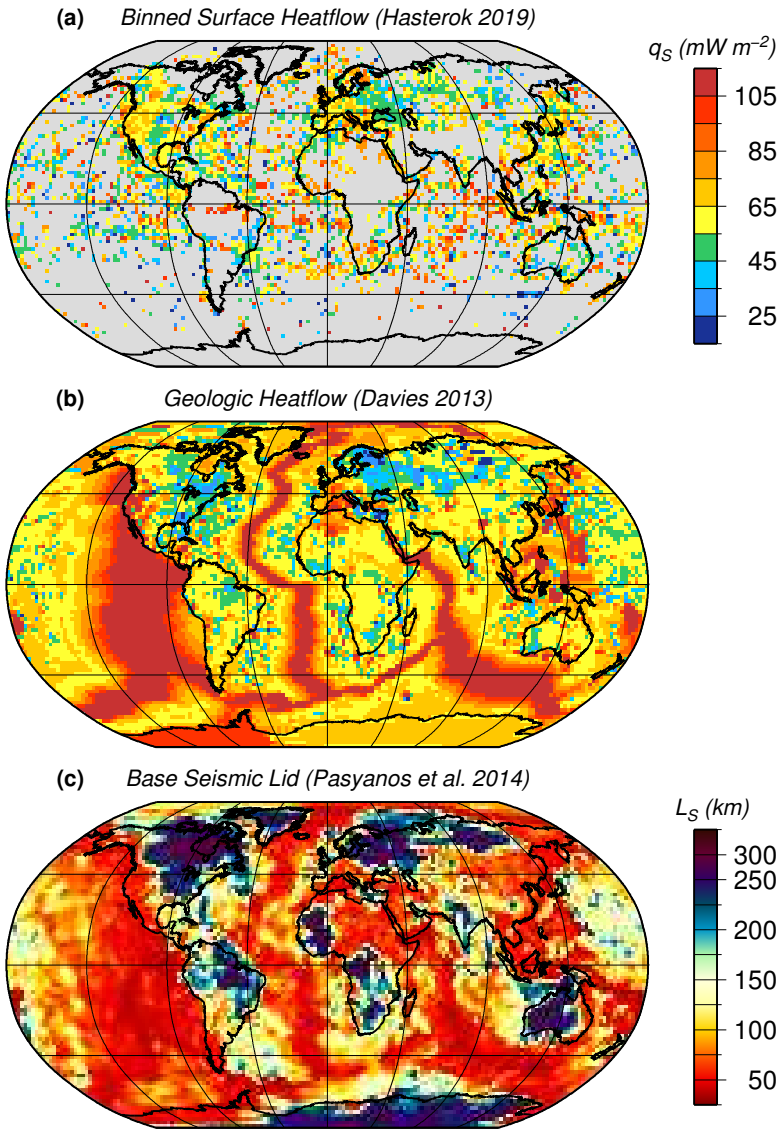

Fig. 1. *(a) Raw surface heat flow data binned on a 2°x2° grid (only values < 120 mWm^{-2} included) (from current global heat flow database, updated from Hasterok and Chapman [2011]). (b) Full global heat flow grid obtained by assigning to cells without data either values based on geologic similarity in continents or based on ocean floor age in oceans (from Davies [2013]). (c) Depth of the base of the seismic lithosphere (from LITH1.0 Pasyanos et al. [2014])*

2. Observational constraints

A range of surface observations provides, mostly indirect, constraints on lithospheric temperatures (**Fig. 2**). In this section, we discuss the main geophysical and geochemical constraints that have led to our current understanding of the thermal state of the continental lithosphere.

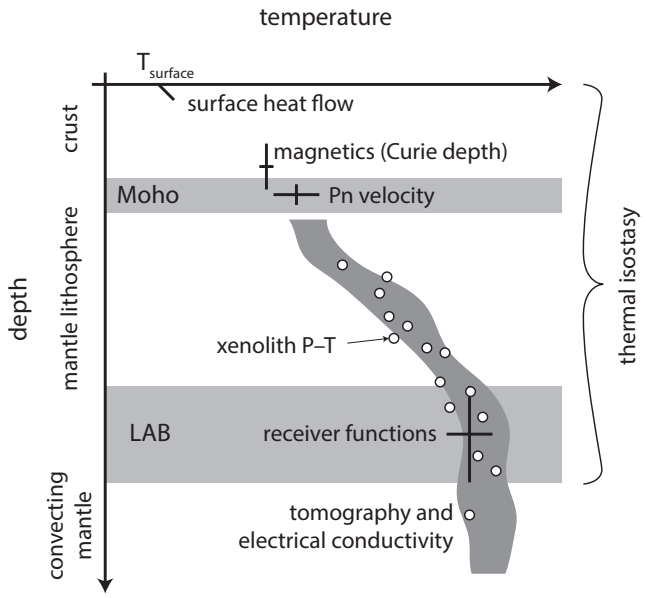

Fig. 2. *A number of indirect methods provide independent information on lithospheric temperatures. Surface heat flow provides a surface constraint. Xenolith thermo-barometry gives point estimates within the mantle lithosphere. Seismic tomography and electrical conductivity provide constraints on temperatures in the mantle lithosphere and asthenosphere. Receiver functions may give constraints on conditions, including the presence of melt, near the lithosphere-asthenosphere boundary, and magnetic Curie depth estimates and Pn velocities yield single point estimates of temperature inside and at the base of the crust, respectively. Thermal isostasy gives an estimate of the integrated thermal buoyancy.*

2.1. Surface heat flow

The most direct expression of the temperatures inside the Earth is the thermal gradient that is measured in the course of a surface heat flow determination. This allows estimating surface heat flow. Thus mapped surface heat flow correlates with tectonics and thermotectonic age, following the lithospheric age pattern in the oceans, and in continents broadly increasing from low values between 30 and 50 mWm^{-2} in Archaean cratons to high values between 60 and 90 mWm^{-2} in tectonically active regions (**Figs. 1**a, **3** [*Pollack et al.*, 1993; *Davies and Davies*, 2010]). The spatial density of measurements is highly variable. Many areas are poorly covered, including much of Africa, South America, the Middle East, Antarctica and Greenland on continents and the South Pacific and Southern Oceans (**Fig. 1**a).

Uncertainties in heat flow measurements are largely due to uncertainties in thermal conductivity and the thermal gradient, which amount to about 10% of the heat flow estimate for conventional methods. Uncertainties are often greater than ~20% for bottom-hole temperature derived estimates, but with large numbers of samples, the statistical uncertainty can be reduced to uncertainties on par with conventional estimates. At some sites, there is an uncertainty in whether surface heat flow reflects the conductive state of the lithosphere or advective heat transport by fluids or melts. The latter uncertainty particularly affects the interpretation of thermal structure in young oceans and near active volcanic regions in continents.

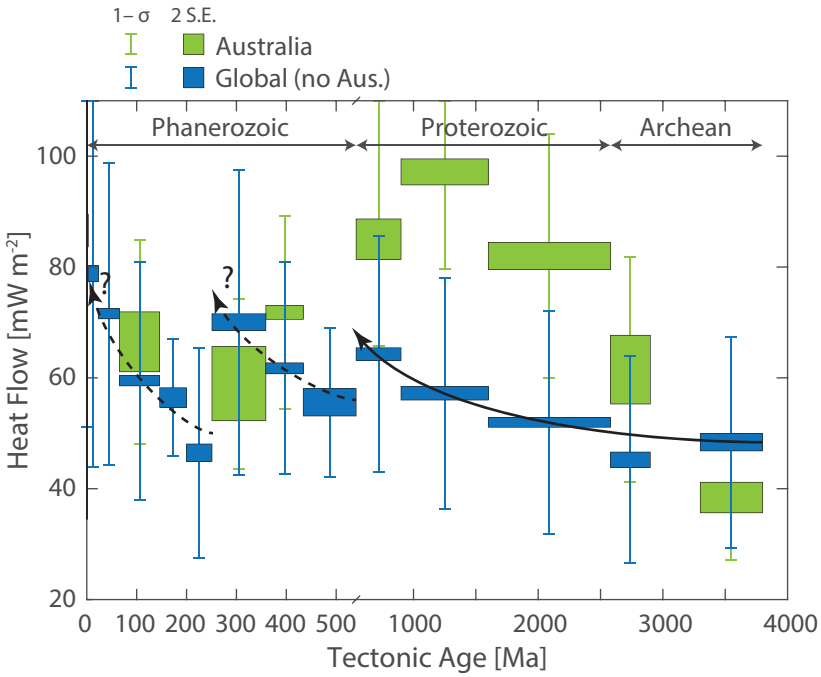

Fig. 3. *Heat flow weakly correlates with tectonic age, as evidenced by the large natural range in heat flow (error bars) whereas the standard error in the mean (boxes) indicates that trends (indicated by arrows) may be resolvable. Australian data, (N=1635, green), are excluded from the global analysis (N=29852, blue) because of their clearly anomalous heat flow [McLaren et al., 2003; Hasterok and Webb, 2017], particularly in the Proterozoic where Australian data constitute an unrepresentative fraction of the total dataset relative to their area.*

Relations between surface heat flow, thermotectonic age and crustal composition have been used to derive estimates of surface heat flow for regions with little or no data [*Pollack and Chapman*, 1977; *Pollack et al.*, 1993; *Davies and Davies*, 2010; *Hasterok and Chapman*, 2011; *Davies*, 2013], an example of which is shown in **Fig 1**b. However, thermotectonic age alone is a weak proxy (**Fig. 1**b and **Fig. 3**) due to the large natural variability in crustal heat production and the style and magnitude of tectonic events. Isostatic, seismic, and magnetic methods can be used to further constrain such maps and estimate plausible temperature-depth distributions [*Shapiro and Ritzwoller*, 2004b; *Maule et al.*, 2005; *Goutorbe et al.*, 2011; *Hasterok and Chapman*, 2011; *An et al.*, 2015; *Martos et al.*, 2017]. Other studies have used surface heat flow and heat production data to extrapolate to temperatures at depth [e.g. *Artemieva and Mooney*, 2001; *Michaut et al.*, 2009], sometimes with additional constraints from seismic data [*Shapiro and Ritzwoller*, 2004b; *Perry et al.*, 2006; *Lévy and Jaupart*, 2011]. Once a global distribution of surface heat flow has been estimated, the total budget of heat loss through the surface of the Earth as well as the relative contributions of oceanic and continental areas to this heat loss can be estimated [*Jaupart and Mareschal*, 2007; *Davies and Davies*, 2010; *Hasterok*, 2013; *Lucazeau*, 2019].

2.2. Petrologic geotherms

Various petrological and geochemical measurements can provide point estimates of lithospheric temperatures. The most important of these are pressure–temperature conditions inferred from xenoliths and xenocrysts, fragments of the mantle or crust brought up by magmatic activity, most notably by kimberlites. Due to the rapid transport by the magmas, these lithospheric rocks often reflect the P,T conditions of their origin before incorporation into the host magma.

A range of thermometers and barometers have been developed for xenoliths that exploit the variable rates of elemental exchange between mineral phases at different temperatures and pressures [e.g. *O'Neill and Wood*, 1979; *Finnerty and Boyd*, 1987; *Brey and Köhler*, 1990; *Taylor*, 1998; *Nimis and Taylor*, 2000]. Uncertainties in these P,T estimates, derived from the reproducibility of experimental results, lie within 0.3-0.5 GPa and 30-180° [*Pearson et al.*, 2003; *Nimis and Grütter*, 2009]. Furthermore, most such barometers rely on the presence of garnet and can therefore only be applied to xenoliths extracted from pressures greater than ~2 GPa. Thermometers are comparatively more plentiful and thus applicable to a wider depth range. However, variations in the oxidation state of the mantle may have considerable impact on temperatures calculated from Fe-Mg exchange [*Canil and O'Neill*, 1996]. This sensitivity to Fe^{3+} may result in large uncertainties of >200 °C as well as disparities between different thermometers, where two-pyroxene thermometers are the most reliable [*Canil and O'Neill*, 1996; *Nimis and Grütter*, 2009; *Matjuschkin et al.*, 2014].

Xenocrysts, single crystals of background lithospheric mantle incorporated into magmas, can also retain a record of their original conditions which, if carefully analysed, has been shown to be consistent with the conditions retrieved from xenoliths [*Ryan et al.*, 1996; *Nimis and Taylor*, 2000; *O'Reilly and Griffin*, 2006; *Grütter*, 2009; *Mather et al.*, 2011; *Bussweiler et al.*, 2017]. As xenocrysts are substantially more plentiful than xenoliths, they can be used to expand and complement the xenolith constraints on pressure, temperature and compositional conditions of the lithospheric mantle.

Such xenotherms, derived from xenolith and xenocryst P,T data, reflect low temperatures in the deep lithosphere below cratons around the world and higher temperatures in areas that have been affected by more recent tectonic activity (**Fig. 4**). Such temperature ranges are consistent with those from steady state conductive geotherms obtained by extrapolating surface heat flow values downward taking into account crustal heat production (for further discussion see below).

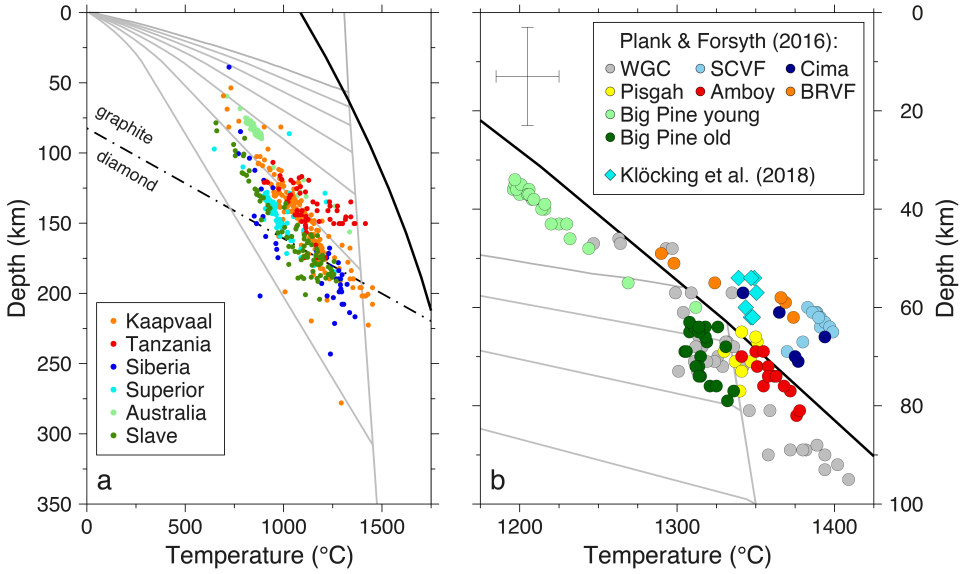

Fig. 4. *(a) Range of P,T conditions from xenoliths from a range of tectonic settings [Garber et al., 2018]. Solid black line = dry solidus [Katz et al., 2003]); dot-dashed line = graphite-diamond transition [Kennedy and Kennedy, 1976]; grey lines = geotherms calculated with surface heat flow every 10 mW m^{-2} between 30 and 90 mW m^{-2} [Hasterok and Chapman, 2011]. (b) P,T estimates for Basin and Range, western US, from geothermobarometry and thermodynamic modelling of mafic volcanic compositions. Circles = Plank and Forsyth [2016]; diamonds = average 'asthenospheric' melts from Klöcking et al. [2018] which include Plank and Forsyth [2016] samples; cross in top left corner denotes approximate uncertainties associated with these estimates. Solidus and geotherms as in left panel*

An outstanding debate is to what extent xenotherms reflect steady state or background thermal conditions. Xenolith/xenocryst occurrences are confined to volcanically active regions. They are therefore concentrated near craton margins and may reflect transient conditions imposed by the heat source that produced the host volcanism [*Bell et al.*, 2003; *Carlson et al.*, 2005; *Eaton et al.*, 2009]. In some locations (most prominently Lesotho in southern Africa), xenotherms show a distinct deflection to high temperatures at depth [*Boyd*, 1973], as might be expected shortly after emplacement of a heat source near the base of the lithosphere (see discussion on geotherms in Section 4 and supplementary material section S2). There has been debate on the reliability of these high temperature estimates [*Bell et al.*, 2003]. However, xenoliths/xenocrysts that yield these high temperatures are also compositionally and texturally distinct, displaying evidence of modification by infiltration of hot fluids or melts [*Griffin et al.*, 2003; *Eaton et al.*, 2009]. Some interpretations of seismic velocities also indicate that xenotherm estimates tend to be higher than present-day lithospheric temperatures and that the high T xenoliths thus probably reflect emplacement conditions [*James et al.*, 2004; *Eeken et al.*, 2018].

The chemical composition of magmas provides an additional dataset that has been used to infer temperatures and thermal thickness of the lithosphere in regions that have been volcanically active [e.g. *McKenzie and O'Nions*, 1991; *Lee et al.*, 2009; *Leeman et al.*, 2009; *Plank and Forsyth*, 2016]. Melt geothermobarometry uses the composition of samples of the most primitive (i.e. least evolved/differentiated) melts,

to infer the P,T conditions where these melts last equilibrated with a mantle source [*Putirka*, 2008; *Lee et al.*, 2009; *Plank and Forsyth*, 2016]. These P,T estimates of last equilibration are generally thought to reflect primary melting conditions, even though this method essentially assumes batch melting and cannot resolve melt generation and accumulation/migration over a range of depths. Furthermore, it has been shown that in part such samples may reflect magmatic pathways and ponding within the lithosphere [*Perrin et al.*, 2016]. Nonetheless, the deepest conditions inferred from the thermobarometry of melts in any given location appear to coincide with where seismic studies would infer the base of the lithosphere [*Kelley et al.*, 2006; *Plank and Forsyth*, 2016], and may thus constrain thermal conditions near the boundary between lithosphere and asthenosphere and thickness variations of the lithosphere.

An alternative method is the thermodynamic modelling of major and trace element composition of melts as a function of source composition and mineralogy, pressure and temperature [*McKenzie and O'Nions*, 1991; *Ghiorso et al.*, 2002; *Brown and Lesher*, 2016]. In contrast to geothermobarometry, this approach can accurately reflect the entire melt path but is reliant on prior knowledge of the mantle source composition (e.g. from isotopic measurements) and the chosen thermodynamic parameters. A further source of uncertainty is whether melting is restricted to the asthenosphere or whether the sub-continental lithospheric mantle may contribute to the final magma composition [*Harry and Leeman*, 1995]. As such, depth estimates from thermodynamic modelling can be considered as minimum constraints on lithospheric thickness.

In the western US, a combined analysis of magma geothermobarometry and surface wave dispersion suggests that the base of the lithosphere below the Basin and Range varies in depth and is largely defined by the dry solidus [*Plank and Forsyth*, 2016] (**Fig. 4**). Estimates of the degree of melting and asthenospheric temperatures from detailed modelling of rare earth element (REE) compositions of basalts from the same region yield similar temperatures and depths and further reinforce that variations in thickness of the lithosphere exert a primary control on thermal structure and mantle melting below this region [*Klöcking et al.*, 2018].

2.3. Geophysical constraints

The most detailed constraints on lithospheric structure come from the analysis of seismic data either in inversions for 2- or 3-dimensional variations in bulk velocities or in mapping of discontinuities. Seismic velocities vary with temperature, composition, phase and the presence of fluids (including water and melt). However, various studies have shown that because of the large variations in temperature in the lithosphere and the very strong temperature sensitivity, the dominant signature in much of the lithosphere is probably thermal [*Goes et al.*, 2000; *Shapiro and Ritzwoller*, 2004a; *Priestley and McKenzie*, 2006], and hence seismic structure should provide significant constraints on lithospheric temperature. Other geophysical parameters such as electrical conductivity, gravity/geoid and magnetic structure are

also significantly sensitive to thermal structure but have similarly strong sensitivities to the presence of conductive fluids/lithologies, to compositional variations in density or magnetic susceptibility, respectively.

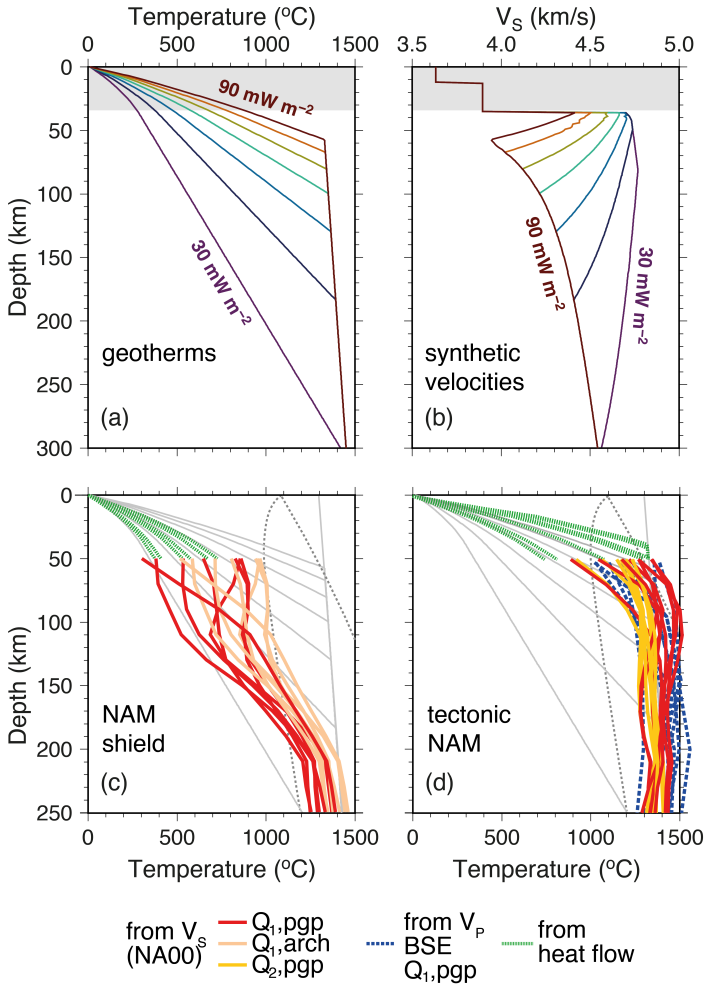

Fig. 5. *(a,b) Reference continental geotherms (with surface heat flow from 30 to 90 mW m^{-2}, every 10 mW m^{-2}, from Hasterok and Chapman, 2011) and corresponding predicted shear-wave velocities assuming (below the crust in gray), an undepleted peridotitic composition and attenuation model Qg [Goes et al., 2012]. The seismic velocity minimum is expected to coincide with the depth where the conductive geotherm intersects the mantle adiabat. (c,d) Seismic geotherms below North America [from Goes and Van der Lee, 2002] inferred from shear velocity model NA00 [Van der Lee, 2002] and P velocity model BSE-NL [Bijwaard et al., 1998]. For reference, light gray lines show the geotherms from (a), dashed gray lines the wet and dry mantle solidus. The effect of major-element composition (pgp – primitive garnet peridotite, arch – depleted Archean mantle composition) is minor, up to 100-150°C for cool lithosphere (c). Anelastic effects (model Q_2 is more strongly temperature sensitive than model Q_1) strongly influence seismic sensitivity to temperature near adiabatic mantle temperatures (d). A range of temperatures and thermal thicknesses similar to the full range of geotherms from (a) is needed to explain the variation in seismic velocities within the continental lithosphere.*

Fundamentally, the lithosphere is the rheologically strong part of the top thermal boundary layer of the convecting mantle [*Anderson*, 1995; *Afonso et al.*, 2016a; *Garel and Thoraval*, 2020]. Due to the exponential dependence on temperature of most rock

rheologies, temperature will in most places exert the primary control on its thickness. The intersection of the conductive geotherm and adiabat is a practical definition of thermal thickness of the lithosphere even if it is expected that there is a transitional boundary layer of up to several 10s of km between the two [*Rudnick and Nyblade*, 1999; *Sleep*, 2003; *McKenzie et al.*, 2005; *Michaut et al.*, 2007]. For steady-state geotherms, the intersection between the conductive geotherm and the mantle adiabat is expected to correspond to a minimum in seismic velocity (**Fig. 5**a,b) (more discussion in, for example, [*Goes et al.*, 2012]). Other geophysical measures (such as velocity discontinuities or changes in conductivity) may reflect structure either within the lithosphere or within the transition zone between lithosphere and asthenosphere, e.g., interfaces where melts/fluids may pond [e.g. *Sim et al.*, 2020] or where anisotropy may change [*Eaton et al.*, 2009; *Kawakatsu et al.*, 2009; *Rychert and Shearer*, 2009; *Fischer et al.*, 2010; *Yuan and Romanowicz*, 2010; *Karato*, 2012; *Naif et al.*, 2013; *Beghein et al.*, 2014; *Afonso et al.*, 2016a; *Hansen et al.*, 2016]. But thickness of the seismic lithosphere as inferred from bulk velocity structure may be a reasonable observational proxy of thermal thickness of the lithosphere [*Van der Lee*, 2002; *Pasyanos*, 2010]. A range of studies have estimated seismic thickness of the lithosphere from tomography [e.g. *Priestley and McKenzie*, 2013; *Pasyanos et al.*, 2014] and as might be expected if it largely reflects thermal structure, seismic thickness broadly correlates with surface tectonics similarly to surface heat flow (**Fig. 1**c).

Various studies have mapped imaged seismic velocities and or attenuation into 3-D temperatures of the mantle lithosphere below the continents either by assuming a composition or simultaneously inverting for one [e.g. *Goes et al.*, 2000; *Goes and Van der Lee*, 2002; *Shapiro and Ritzwoller*, 2004a; *Goes et al.*, 2005; *Deen et al.*, 2006; *Priestley and McKenzie*, 2006; *Khan et al.*, 2011; 2013; *Priestley and McKenzie*, 2013; *Hirsch et al.*, 2015; *Dalton et al.*, 2017; *Eeken et al.*, 2018; *Schutt et al.*, 2018](**Fig. 5**). Alternatively, joint inversions for temperature and composition have been done by adding constraints from gravity to the inversion [e.g. *Godey et al.*, 2004; *Van Gerven et al.*, 2004; *Tesauro et al.*, 2014], or by combining a wider range of observations in a joint inversion [*Afonso et al.*, 2013b; *Afonso et al.*, 2013a; *Afonso et al.*, 2016b; *Plank and Forsyth*, 2016; *Jones et al.*, 2017]. Other contributions in this special issue discuss this mapping and the uncertainties associated with it. Largely, the results from such studies are consistent with continental geotherms from petrology (Section 2.2) and steady-state heat-flow based families discussed in Section 4. Figure 5 (c,d) shows the temperatures inferred from two North American seismic velocity models [*Goes and Van der Lee*, 2002] under the assumption that all velocity variations are due to thermal structure. The seismic geotherms span the full range of temperatures of geotherm families with surface heat flow between 30 and 90 mW m^{-2}. The inferred range in thermal thicknesses from more than 200 km in the eastern US, to as low as 50 km below the western US agrees with analyses of more recent velocity models [e.g. *Klöcking et al.,* 2018].

In analyses like this, composition has usually been allowed to vary between a fertile, peridotitic, mantle composition and the more refractory harzburgitic to dunitic

compositions that are commonly found in xenoliths below old cratons. Although seismic constraints have limited sensitivity to compositional variations in this range, and hence temperature estimates are not strongly affected [*Goes et al.*, 2000; *Schutt and Lesher*, 2006], xenoliths, gravity and geoid do require systematic variations in average composition of the lithospheric mantle between older and younger parts of the continental lithosphere. Most geophysical imaging to date cannot achieve sufficient depth resolution to confidently resolve deviations from standard steady-state geotherms. Multi-observation inversions that include data sensitive to a range of geophysical parameters including to bulk seismic as well as seismic discontinuity structure, with geodynamic and thermodynamic constraints are a promising method to resolve tradeoffs and achieve higher resolution estimates of continental temperatures [*Afonso et al.*, 2013b; *Afonso et al.*, 2013a; *Afonso et al.*, 2016b]. Below (Section 4.4), we will discuss an example of how temperatures inferred from Pn waves that travel just below the Moho can further constrain geotherm shapes.

Magnetic data may provide additional constraints on crustal temperatures. Crustal minerals lose their spontaneous magnetisation once they cross the Curie temperature. This temperature is about 580°C for magnetite which is likely the dominant magnetic mineral in much of the continental crust. Maps of magnetic anomalies at the surface can be inverted for the depth extent of magnetic sources, which can then be used as a proxy for the Curie depth, and with an assumption of the responsible mineral, a temperature at depth. Such maps correlate quite well with surface heat flow, confirming that they provide a useful temperature proxy [e.g. *Bouligand et al.*, 2009; *Chopping and Kennett*, 2015; *Mather et al.*, 2019].

Magnetotelluric data that can be used to map electrical conductivity with depth are another independent source of temperature constraints. Electrical conductivity is particularly sensitive to the presence of fluids, the presence of other highly conductive minerals (e.g. graphite) and temperatures. Depending on the measurement periods, it can be used to map structure throughout the mantle lithosphere and into the asthenosphere. Such data have sometimes been included in inversions for lithospheric temperatures [*Afonso et al.*, 2016b; *Jones et al.*, 2017]. These data and their strengths and limitations are discussed in detail in the paper by *Naif et al.* [2020].

3. Heat transfer and thermal parameters

In a thermal sense, the lithosphere constitutes the conductive upper boundary layer of the convective mantle. For much of the lithosphere, one-dimensional solutions to the equation for heat transfer (Supplement) that consider just vertical heat conduction are good approximations because vertical thermal gradients tend to be much larger than horizontal ones apart from near steps in lithospheric thickness. For oceanic lithosphere, solutions that balance vertical conduction with horizontal advection due to plate spreading provide very good thermal reference models [*Richards et al.*, 2020].

Thermal structure of the continental lithosphere is determined by three main contributions: (i) crustal heat production, (ii) heat flow from the mantle, which is largely governed by/reflected in thermal thickness of the lithosphere with some potential modulation by heat production in the lithospheric mantle and (iii) non-steady state contributions.

3.1. Steady vs. non-steady state

Continental lithospheric temperatures are commonly assumed to be steady state, i.e., heat flow out of the surface is in balance with the heat flow that is advected into the base of the lithosphere and the heat produced by radioactive decay inside the lithosphere. The time scale to reach steady state is about 300 m.y. for a 100 km thick lithosphere and may be as low as 50 m.y. if most heat production is concentrated in the upper 40 km of the lithosphere [*Pollack and Chapman*, 1977; *Jaupart and Mareschal*, 2007]. Although, due to the evolution of heat production by radioactive decay, even old lithosphere may never reach a complete steady state [*Michaut et al.*, 2009], steady-state approximations are appropriate for large parts of the lithosphere that have been tectonically undisturbed for tens to hundreds of millions of years (as indicated by compilations of lithosphere and basin ages, e.g. as discussed by [*Goutorbe et al.*, 2011]).

Furthermore, many common processes, such as lithospheric thickening, thinning or instantaneous heating at the base (e.g. by a mantle plume), result in transient geotherms with similar monotonous shapes as the steady state geotherms (Supplementary **Fig. S2-S4**). An exception are the strongly perturbed geotherms that can form by thrust tectonics where the lithosphere is significantly thickened, although even these geotherms relax towards a monotonous shape within a few tens of millions of years (Supplementary **Fig. S3**). Thus, unless very recent, deviations from steady-state shapes would be difficult to distinguish with most geophysical observations that are only sensitive to averaged or integrated thermal structure. Hence, even time-dependent thermal state can be described with steady-state geotherms, so long as one bears in mind that the effective heat production inferred could be larger or smaller than actual heat production in non-steady state conditions.

3.2. Thermal conductivity

Thermal conductivity, k, is the rate at which heat is transferred a unit distance per degree of temperature difference whereas the thermal diffusivity κ is the ratio of the rate at which a material conducts thermal energy to its capacity to store heat. The thermal diffusivity and thermal conductivity are related by $\kappa = k/\rho C_P$, where ρ density and C_P specific heat. Variability and uncertainties in thermal conductivity contribute to uncertainties in: (a) the estimate of surface heat flow via Fourier's law (i.e. $q = k\, dT/dz$), and (b) the extrapolation to temperatures at depth assuming a conductive equilibrium. Thermal diffusivity variations are very similar to those of thermal conductivity. While density and specific heat capacity are also temperature and

pressure dependent, the heat capacity, ρC_P, is generally fairly constant [*Vosteen and Schellschmidt*, 2003]. Hence thermal conductivity variations are the dominant control on diffusivity.

Thermal conductivity is dependent on the mineralogical constitution of a rock and the physical state (P and T). At room temperature, the average thermal conductivity for most intermediate and mafic igneous rocks is relatively similar (~2.5 W m^{-1} K^{-1}). Due to the exceptionally high thermal conductivity of quartz (7 to 8 W m^{-1} K^{-1}; [*Horai*, 1971]), the conductivity of felsic igneous rocks is generally controlled by the volume fraction of quartz (**Table 1** and extended in **Table S1**). Like plutonic rocks, the thermal conductivity of volcanic and sedimentary rocks is highly dependent on the volume fraction of quartz but there is also a strongly dependence upon porosity due to the very low thermal conductivity of most pore fluids relative to the rock matrix. Thermal conductivities of the mantle lithosphere are generally higher than the crust.

Many thermal models use an upper crustal thermal conductivity of 3 W m^{-1} K^{-1} for the upper crust, but this may be too high. Conductivity estimates for average upper crustal compositions suggest the upper crust is more likely granodioritic in composition and therefore an average surface thermal conductivity of ~2.7 W m^{-1} K^{-1} may be more reasonable (**Table S2**). Estimates of lower crustal conductivities derived from average geochemical models are ~2.5 W m^{-1} K^{-1} at laboratory ambient laboratory conditions.

Thermal conductivity strongly decreases with temperature and weakly increases with pressure (e.g., **Fig. 6** for olivine), although there are a few minerals for which conductivity increases with temperature (e.g., β-quartz and feldspars [*Höfer and Schilling*, 2002; *Petrunin et al.*, 2004]). The thermal conductivity of most crustal rocks converges at higher temperature to values between ~2 and 2.5 W m^{-1} K^{-1} [*Zoth and Hänel*, 1988; *Vosteen and Schellschmidt*, 2003]. *Hasterok and Chapman* [2011] developed a P–T-dependent mineralogy-based model that is accurate for a number of crystalline rocks, but it is severely limited by the number of minerals that have been studied in detail. Their model can be cumbersome to compute and requires an estimate of the mineralogy (and solid solution proportions), which is generally unknown. A number of empirical T-dependent conductivity models have been developed over the past 40 years, each calibrated to a small subset of laboratory measurements, but no model explains all the data well. Although there is no simple mathematical form for the change in thermal conductivity with P–T conditions, the general behavior can be approximated by:

$$k_{\text{eff}} = k_1 + k_2,$$
$$k_1 = \frac{k_0(n-1)}{n}(1 + \beta P),$$
$$k_2 = k_0 \exp\left(-\frac{T-25}{300}\right),$$

where k_0 is the room-temperature conductivity estimate (e.g., **Table 1**), T is in ºC, P is in GPa, β is the pressure coefficient (0.1 GPa^{-1}) and n is an empirical factor, $n = 6.4 - 2.3 \log k_0$.

		SiO_2			density		P-wave velocity		Thermal conductivity		heat production[b]									
											< 2 Ga					> 2 Ga				
Rock type[a]	N	M[d]	min	max	μ	σ	μ	σ	μ	σ	N	μ	σ	μ_{ln}	σ_{ln}	N	μ	σ	μ_{ln}	σ_{ln}
			wt. %		kg m^{-3}		km s^{-1}		W m^{-1} K^{-1}		μW m^{-3}									
subalkaline																				
granite	27192	73.9	69	86.7	2661	34	6.16	0.07	2.89	0.16	11681	3.27	3.91	0.91	0.75	2111	2.82	7.41	0.49	0.97
granodiorite	9146	67.3	63	76.5	2722	36	6.40	0.09	2.68	0.12	4241	1.67	1.83	0.27	0.71	1000	1.05	1.65	-0.32	0.84
diorite	3934	60.4	57	63	2795	43	6.65	0.11	2.47	0.10	2037	1.05	0.95	-0.19	0.71	238	0.71	0.56	-0.66	0.86
gabbroic diorite	4743	53.8	52	57	2903	53	6.95	0.16	2.37	0.12	1951	0.67	1.98	-0.81	0.86	445	0.43	0.45	-1.14	0.80
subalkalic gabbro	5471	50.3	45	52	2956	45	7.12	0.16	2.29	0.09	1974	0.33	0.45	-1.56	0.99	878	0.25	0.77	-1.91	0.98
peridotgabbro	341	43.5	41	45	3034	80	7.42	0.25	2.14	0.10						47	0.27	0.47	-2.21	1.31
alkaline																				
quartz monzonite	4355	66.4	61.2	71.1	2689	43	6.35	0.09	2.50	0.10	2219	2.72	2.97	0.78	0.63	305	2.36	5.88	0.32	0.81
syenite	1356	62.7	57.7	71.1	2662	52	6.35	0.11	2.20	0.13	623	4.05	3.99	1.05	0.82	39	2.77	2.23	0.76	0.71
monzonite	2809	58.6	53.2	63	2764	36	6.62	0.11	2.28	0.12	1380	2.14	2.98	0.45	0.73	146	1.26	1.18	-0.11	0.84
monzodiorite	1933	53.5	49.5	57	2843	38	6.82	0.13	2.18	0.11	776	1.33	1.60	-0.04	0.80	100	0.98	1.07	-0.40	0.91
monzogabbro	678	49.7	45.2	51.9	2907	34	6.96	0.13	2.09	0.08	271	1.07	4.14	-0.45	0.76	43	0.79	1.05	-0.65	0.90
alkalic gabbro	1900	48.2	45	51.9	2951	41	7.05	0.12	2.13	0.07	753	0.46	0.58	-1.06	0.73	169	0.37	0.32	-1.31	0.85
high-magnesian																				
mantle peridotite	1204	43.9	33.5	45	3323	35	8.13	0.11			98	0.13	0.38	-3.08	1.22	41	0.05	0.06	-3.45	0.96
mantle pyroxenite	79	43.5	33.5	45	3204	81	7.81	0.20			35	0.09	0.11	-2.90	1.08	6	0.09	0.07	-2.66	0.70
sedimentary																				
											combined[c]									
quartzite	2231	89.2	72.5	99.8	2688	48					2231	1.74	4.69	-0.09	1.02					
quartz arenite	94	69.3	15.8	99.9	2960	212					94	0.62	2.58	-2.13	1.71					
litharenite	689	76.6	44.1	91.3	2734	58					689	2.50	4.46	0.57	0.68					
sublitharenite	86	75.5	44.8	97.2	2819	91					86	1.40	1.38	0.01	0.82					
arkose	1315	73.2	45.2	91.3	2684	74					1315	2.97	4.60	0.76	0.68					
subarkose	173	75.2	56.4	97.2	2765	91					173	2.25	5.34	0.17	0.84					
wacke	3859	70.5	38.1	85.8	2716	49					3859	2.71	4.44	0.72	0.60					
iron-rich sand	802	66.0	3	97.7	2897	154					802	2.79	7.72	0.06	1.27					
shale	4129	62.8	7.1	78.4	2749	45					4129	2.56	3.70	0.70	0.60					
iron-rich shale	2579	56.9	0.3	81.1	2861	84					2579	1.47	4.52	-0.15	0.83					
limestone	1554	29.8	0	57	2717	72					1554	1.48	5.17	-0.93	1.31					
dolomite	1227	32.3	0	61.9	2789	53					1227	1.69	6.30	-0.38	1.15					

[a]Plutonic rocks are estimated from total alkali-silica classification and IUGS high-magnesium classification [*Middlemost*, 1994] and sedimentary rocks are estimated using Sandclass [*Herron*, 1988]; [b]estimates < 2 Ga exclude Australian data between 2.0 and 1.4 Ga; [c]sedimentary averages are independent of age; [d]median value

.

Table 1 (previous page) - *Physical properties of common rock types estimated from global geochemical compositions. Density model from Hasterok et al. [2018]; V_P model from Behn and Kelemen [2003]; heat production from Rybach [1988]; and thermal conductivity from Jennings et al. [2019].*

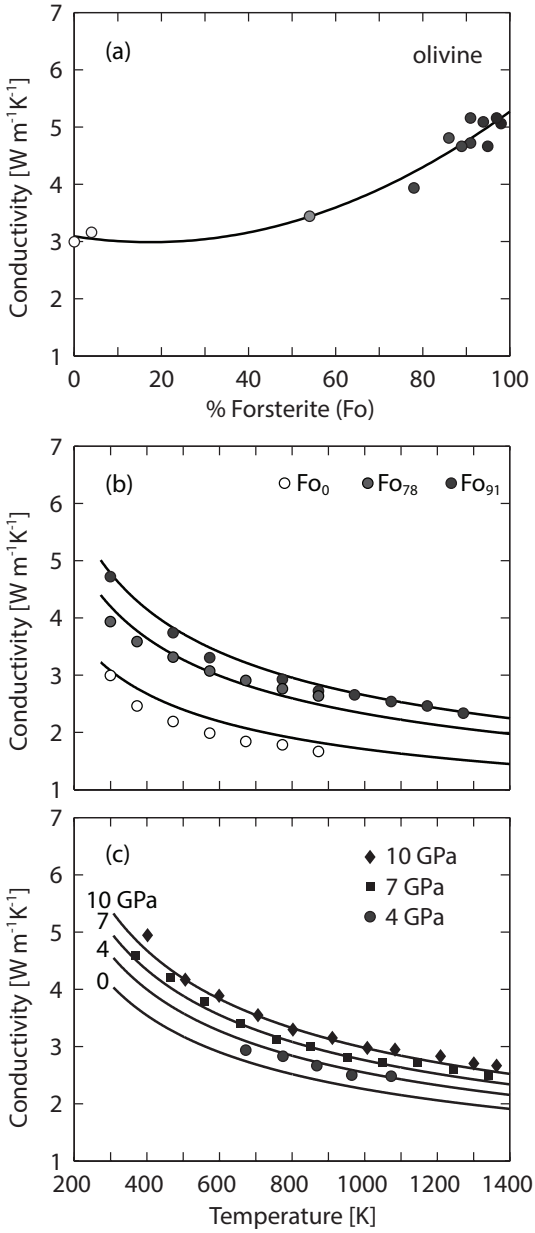

Fig. 6. *Thermal conductivity of olivine. (a) Variations in thermal conductivity as a function of composition ranging from pure fayalite (Fe_2SiO_4) to pure fosterite (Mg_2SiO_4). (b) Thermal conductivity variations as a function of (b) temperature and composition and (c) temperature and pressure. Data from Horai and Simmons [1969]; Horai [1971]; Harrell [2002]. The olivine thermal conductivity model is given by $k(P,T) = (3.09 - 1.17\ Fo + 3.35\ Fo^2)\ (298\ T^{-1})^{0.49}(1 + P\ K_T'\ K_T^{-1})$ where P and T are pressure and temperature, Fo is the fraction of fosterite, K_T and K_T' are the isothermal bulk modulus and its first pressure derivative.*

Thermal conductivity is a macroscopic physical parameter used to describe the effect of two subatomic processes, the transfer of vibrational energy from one bond to another (phonon-phonon transport) and vibrational energy converted to light (phonon-photon). The former is known as lattice thermal conductivity and the former as radiative thermal conductivity. Early experiments suggested radiative transport represented a significant fraction of heat loss at temperatures above ~500 K [*Schatz and Simmons*, 1972] However, more recent studies have called this into question. It is quite possible that the radiative contribution is negligible, at least within the lithosphere and upper mantle [*Hofmeister*, 1999]. Earlier geotherms computed with

the earlier radiative models result in geotherms that are strongly curved in the lower lithospheric mantle [e.g. *Chapman*, 1986] whereas geotherms computed with more recent radiative estimates result in higher estimated lithospheric mantle temperatures [*Hasterok and Chapman*, 2011].

3.3. Crustal Heat Production

Heat production is one of the least constrained physical properties within the lithosphere because heat producing elements (HPEs) are trace elements found in accessory mineral phases that do not affect macroscopic geophysical properties that can be remotely sensed from the surface (e.g., density, seismic velocity, electrical resistivity [*Artemieva et al.*, 2017]). As a result, constraints on heat production are generally indirect. Most of our understanding of heat production come by two means: direct measurements on surface samples, either using gamma-ray spectroscopy or chemical assay; and indirect estimates that incorporate surface heat flow constraints. The former yields limited information on depth, aside from the rare xenolith or oblique terranes that can be used to infer depth but do not necessarily represent the present depth. Heat-flow based observations are sensitive to the integration of heat production over depth but the resolution is limited and can be difficult to separate from mantle heat flow. More recently, seismic methods, Curie depth estimates and gravity/isostasy have been used to improve constraints on heat production, but these techniques often explore a model space that is established by chemical or heat flow observations. These unconventional methods are addressed in the latter sections of this paper.

3.3.1. Sources of heat production

Heat production results from the decay of radiogenic isotopes within the crust, the most important of which are the decay series ^{40}K, ^{232}Th, ^{235}U and ^{238}U [*Rybach*, 1988]. The additional isotopes ^{87}Rb and ^{144}Sm generally contribute <1% to the total production. Volumetric heat production is determined by:

$$A = 10^{-5}\,\rho(3.4302\,C_{\mathrm{K}} + 2.6368\,C_{\mathrm{Th}} + 9.8314\,C_{\mathrm{U}}), \qquad (1)$$

where A is in μW m^{-3}, ρ is in kg m^{-3}, and C is the concentration with K in wt.% and Th and U in ppm [*Ruedas*, 2017].

Models of average crustal composition by *Rudnick and Gao* [2003] yield heat production estimates for the upper, middle, and lower crust of 1.66±0.17 (1σ), 0.99±0.11 (1σ), and 0.20 μW m^{-3}, respectively.

Heat production values are not measured directly but are instead computed using experimental results determined from nuclear physics and measurements of elemental concentrations from chemical analyses or gamma-ray spectrometry. The heat produced results from conversion of mass to energy during decay. However, approximately 1/3 of the energy produced during β^- decay is lost to the production of antineutrinos [*Rybach*, 1988]. These so-called geoneutrinos lead to the exciting new

avenue of research into geoneutrinos, which provide a remote sensing method that has the potential to improve estimates of the global radiogenic heat budget [*Dye*, 2012].

3.3.2. Heat-flow based insights

Excellent reviews of heat flow constraints on heat production are given by *Jaupart and Mareschal* [2014] and *Jaupart et al.* [2016]. Here we add some additional insights but refer the reader to these papers for a thorough treatment.

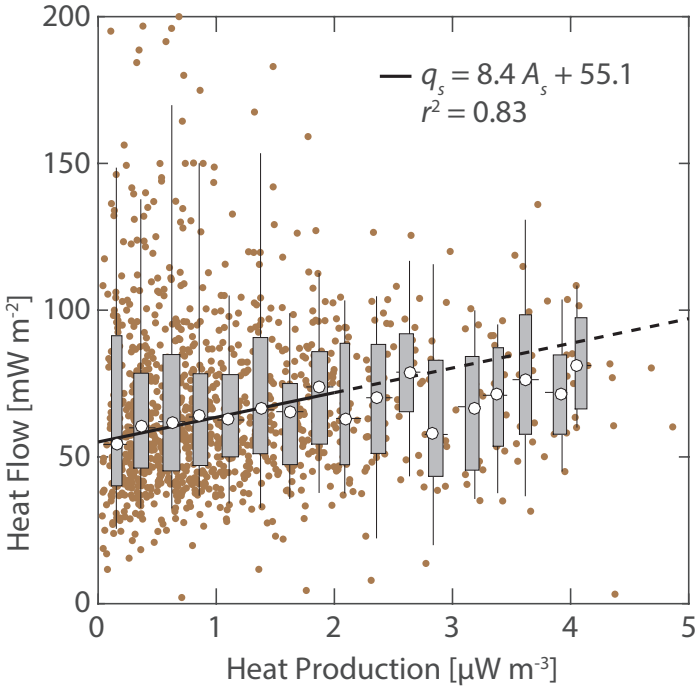

Fig. 7. *The tenuous relationship between heat production and heat flow. The points are average surface heat production and surface heat flow geographic cells approximately 220 × 220 km^2. Only continental igneous samples are used to estimate average heat production as sedimentary and metasedimentary rocks typically represent a small fraction of the total crustal volume. Heat flow and heat production are poorly correlated (points), but binning cells suggests that average heat flow (white circles) systematically increases up to 2 μW m^{-3} at which point there are too few points to produce reliable averages. The grey boxes represent the interquartile range and error bars span the 0.05 to 0.95 quantiles. The basal heat flow predicted from this analysis is a reasonable 55.1 mW m^{-2} and a characteristic depth of 8.4 km consistent with numerous reduced heat flow analyses [Artemieva and Mooney, 2001]. Our characteristic depth is nearly identical to the value obtained by Pollack and Chapman [1977]). However, the scatter in the individual cells suggests one cannot rely on this relationship to provide an accurate heat production or heat flow, given the other.*

Many proposed continental geotherm studies rely on a partitioning of surface heat flow between an enriched upper crustal layer and a basal heat flow into the enriched layer [*Chapman*, 1986; *Artemieva and Mooney*, 2001; *Hasterok and Chapman*, 2011]. This approach is a theoretical construct. The basal heat flow is not the same as a sublithospheric heat flow as it includes the radiogenic contributions of the mantle lithosphere and lower crust, and the enriched upper layer does not correspond to a particular structure or depth in the crust. These models have a long lineage dating to early reduced heat flow studies [*Roy et al.*, 1968; *Lachenbruch*, 1970]. Although,

reduced heat flow analyses are problematic on small spatial scales [*Huestis*, 1984; *Nielson*, 1987; *Sandiford and McLaren*, 2002], they appear to be more reasonable on a province scale [*Pollack and Chapman*, 1977; *Mareschal and Jaupart*, 2004; *Blackwell and Thakur*, 2007]. Globally, we find that the relationship between surface heat flow and surface heat production is very noisy, but on average a systematic increase in heat flow with increasing heat production is observed (**Fig. 7**). The commonly used exponential decrease in heat production with depth was developed to satisfy differential erosion while preserving a linear heat flow–heat production relationship. While heat production may deviate from this exponential model, there are possibly other reasons that it is reasonable as discussed in Section 3.3.3.

The contribution of crustal heat production to continental heat loss has been estimated by combining available data on heat production and studies that reconciled the range of observed global surface heat flow values with xenotherms (xenolith-derived geotherms) and thermal thicknesses inferred from seismic observations. Such studies have shown that on average crustal heat production accounts for 25 to 40% of surface heat flow [*Pollack and Chapman*, 1977; *Artemieva and Mooney*, 2001; *Hasterok and Chapman*, 2011; *Mather et al.*, 2011; *Jaupart and Mareschal*, 2014]. Additionally, the data require heat production to generally decrease with depth, as surface crustal heat production values are generally too high to reconcile with temperatures at depth inferred from mantle-xenolith geothermobarometery (high heat production leads to strong geotherm curvature and predicts deeper temperatures that are too low). High near-surface heat production integrated over the depth extent of the crust would also produce heat flows larger than observed, providing further evidence that heat production must diminish with depth.

3.3.3. Constraints from surface samples

Surface measurements of heat production can be made on an outcrop or down-hole using a γ-ray spectrometer (GRS), or on hand specimens using GRS or a chemical assay technique. X-ray fluorescence (XRF) and inductively-coupled plasma mass spectrometry (ICP-MS) are the most common hand-sample analyses, typically performed during petrogenetic studies. In-situ GRS measurements are faster, cheaper and provide better averages over larger spatial scales than hand samples, but typically have lower sensitivity than XRF to K and ICP-MS to Th and U. As a result, GRS may not provide reliable estimates of heat production on mafic and ultramafic samples (**Table 2**). This low sensitivity is especially true for U, which has a single peak in the γ-ray spectrum that interferes the side lobe of the Th peak. XRF similarly suffers from low sensitivity of Th and U (**Table 2**), but HPE observations are obtained simultaneously with major element determination. Measurements using ICP-MS can resolve U and Th concentrations <0.01 ppm and are therefore suitable for low heat-producing mafic and ultramafic samples. While geochemical measurements are more susceptible to nugget effects than GRS on outcrops, broad elemental analysis allows for a deeper understanding of petrogenetic controls on heat production.

Method	K	Th	U	Reference
GRS	0.03	0.3	0.2	[*Chiozzi et al.*, 2000]
XRF	0.0007	9	6	typically reported
ICP-MS	0.1	0.002	0.005	ALS Minerals (2013)

Table 2. *Typical detection limits for heat producing elements*

Most studies that measure heat production are focused on characterizing the heat production of rock types in the vicinity of heat flow determinations. The collection of these heat production estimates is generally used to establish average surface heat production estimates for reduced heat flow analysis (as described in Section 3.3.2). Through thousands of such analyses, it is clear that heat production increases as a rock becomes more felsic [e.g. *Artemieva*, 2006; *Vilá et al.*, 2010; *Hasterok and Webb*, 2017]. However, most of these studies use GRS observations and reported rock names, which limits the analyses one can make of the controlling influences.

Global chemical reference models can provide average estimates of heat production in crustal layers. Based on such models, estimates of upper crustal heat production range from 1.25 to 1.74 μW m^{-3}, middle crust from 0.93 to 1.31 μW m^{-3} and lower crust from 0.12 to 0.86 μW m^{-3} with an average of 0.41 μW m^{-3} (**Table S2**). However, heat production can be highly variable as it varies with rock type, degree of fractionation, age, and potentially other complex factors.

Estimates of heat production for a number of common rock types derived from a compilation of global geochemical data are given in **Table 1**. Heat production for individual rocks are typically log-normally distributed with a range of about one order of magnitude. For igneous rocks, average heat production increases systematically with increasing silica content and increases with potassium content (**Fig. 8**a-c). Sedimentary rocks also show a compositional dependence on the relative fraction of clay, quartz and carbonate. Carbonates as well as high purity quartz sands tend to be the least heat producing. Heat production is typically highest among shales, particularly iron-rich shales, due to the concentration of heat-producing elements in these units (**Fig. 8**d-f).

There is a general association between the concentration of HPEs and silica content in igneous and meta-igneous rocks that may yield a correlation with seismic velocity and density when there are a sufficient number of observations to see through the large natural variability in heat production [*Hasterok and Webb*, 2017]. While this relationship is not causal, it is a result of magmatic differentiation, which tends to increase large-ion lithophile elements (LILE) as a melt becomes more felsic. The result is a correlation between seismic velocity and heat production that may vary somewhat from region to region depending upon the general alkalinity of the crust and the distribution of ages of rocks.

Heat production not only varies with rock type, but generally increases with decreasing crystallization age [*Artemieva et al.*, 2017; *Gard et al.*, 2019b; *Hasterok et al.*, 2019]. The most comprehensive analysis, by *Gard et al.* [2019b], finds an increase in heat production of ~4-fold from the Archean to ca. 2 Ga, and a relatively constant heat production from 2Ga up to the present. This age pattern is generally

independent of igneous rock type. Looking at only granites, *Hasterok et al.* [2019] found the heat production variation can largely be explained by shifts or variations in the bulk composition. For instance, many of the variations at ages <2.0 Ga appear to correlate well to the relative proportion of ferroan to magnesian granites, with ferroan granites typically more fractionated and higher heat producing. Ancient granites (>2.0 Ga) are more calcic and significantly less heat producing and may be associated with trondhjemite-tonalite-granodiorite (TTG) related processes.

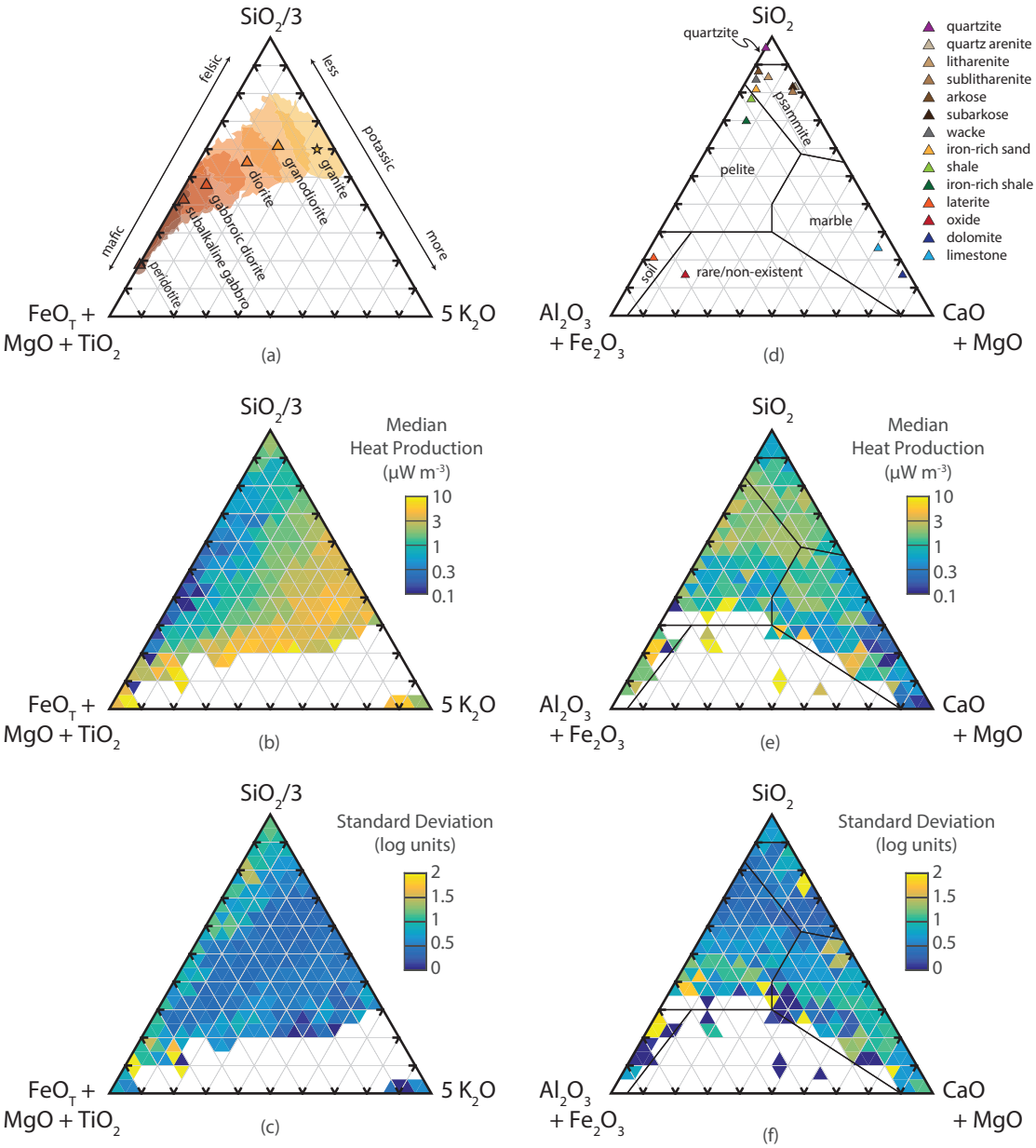

Fig. 8. *Heat production variations with composition (a-c, igneous and metaigneous; d-f, sedimentary and metasedimentary). (a) Fields of common igneous rock types defined by total alkali—silica content [Middlemost, 1994]. The symbols identify the median composition. (b) Heat production and (c) standard deviation of igneous and metaigneous samples. (d) Classification of sedimentary rocks fields [Mason, 1952; Turekian and Wedepohl, 1969]. The symbols identify the median compositions of sedimentary rocks classified by Herron, 1988. (e) Heat production and (f) standard deviation of sedimentary and metasedimentary samples. After Hasterok et al. [2018].*

Most heat production measurements are for upper crustal rocks, complemented by a few outcrops and xenoliths that sample deeper (including lower) crust. Petrological and geochemical arguments as well as geotherm models that have been fit to xenolith P–T estimates bracket characteristic heat production for the mantle lithosphere [*Rudnick et al.*, 1998; *Artemieva*, 2006; *Hasterok and Chapman*, 2011; *Jaupart and Mareschal*, 2014]. Upper crustal heat production is in general a factor 1-3 higher than lower crustal heat production, because upper crust tends to be more felsic. And crustal heat production is 1-2 orders of magnitude higher than that of the mantle lithosphere. Although we find an average heat production of mantle peridotite as 0.1 μWm^{-3}, this value is probably enhanced by metasomatism of the xenolith samples [*Rudnick et al.*, 1998]. More typical estimates are lower 0.01 to 0.04 μWm^{-3} [*Rudnick et al.*, 1998; *Hasterok and Chapman*, 2011], consistent with our median estimates (**Table 1**).

3.4. Estimating regional-scale thermal properties

While heat production has large natural variability, the average heat production on a regional scale tends to correlate with major-element composition and therefore can be reasonably predicted using geology and/or geophysical properties. In **Table 1,** we provide an estimate of geophysical properties, including heat production and thermal conductivity, for a number of common rock types. These estimates can be used as a means to predict thermal properties. The properties are computed from a global geochemical database using empirical predictions based on major-element composition for density, P-wave velocity and thermal conductivity [*Gard et al.*, 2019a]. Heat production is computed from the U, Th and K concentrations of the samples. Australian samples in the range 2.0 to 1.4 Ga are excluded from the heat production estimates because they are significant outliers [*Gard et al.*, 2019b].

Although there is large variability in global heat production estimates for individual rock types, because of the log-normal nature of the distribution of heat producing elements, the regional variations are typically much smaller. *Hasterok and Webb* [2017] suggest that there is often a large reduction in heat production variability from the global scale (σ = 0.5 log-units) to regional scale (σ = 0.1 log-units). A preliminary analysis of modern arcs indicates a similarly low variability in heat production, with a significant correlation between mafic and felsic rocks produced within the same arc. The largest controlling factor on arc heat production appears to be crustal thickness, which is reasonably well correlated with the average heat production of an arc [*Hasterok et al.*, 2020].

To produce reasonable estimates of heat production for estimating heat flow and/or crustal temperatures there are four key observables that can improve heat production estimates. First is the rock type, especially the average felsic to mafic composition of the upper crust and the degree of potassium enrichment [*Hasterok and Webb*, 2017]. Second is the age of the igneous crust, as rocks older than 2.0 Ga tend to have lower heat production, independent of rock type [*Gard et al.*, 2019b; *Hasterok et al.*, 2019]. Third is the thickness of the crust when it formed, as thicker crust tends to be more heat producing independent of rock type [*Hasterok et al.*, 2020]. And fourth is the

vertical distribution of heat production, which may be inferred from seismic velocity [*Hasterok and Webb*, 2017] or the surface heat production, as mafic and felsic heat production are correlated [*Hasterok et al.*, 2020]. One caveat is that these predictors tend to overestimate the crustal heat production when used to model geotherms, but the extent of this effect is unclear. The observations in metamorphic terranes suggest heat production may not decrease with increasing metamorphic grade when controlled for lithology [*Alessio et al.*, 2018; *Hasterok et al.*, 2019], which is contrary to observations made in xenoliths [*Rudnick and Gao*, 2003].

One must be somewhat mindful of the geologic history when utilizing heat production predictors. For example, many terranes within Australia are significant heat production anomalies relative to the global average [*Hasterok and Webb*, 2017], which results in similarly high heat flow (**Fig. 3**). Many terranes once connected to Australia have similarly high heat production. For example, the Namaqua-Natal Belt in southern Africa, the Wopmay Orogen in northern Canada, and the Mawson Craton in east Antarctica all exhibit high heat production [*Flück et al.*, 2003; *Andreoli et al.*, 2006; *Carson et al.*, 2013]. Sediments derived from Australia may also affect crustal heat production in old (Athabasca Basin) and young crust (Banda Arc).

4. Continental Geotherms

4.1. Analytical 1-D steady state geotherms

Analytical 1-D steady-state solutions where the heat production and surface or Moho heat flow are varied independently, serve as a useful parameterization of thermal structure where it is reasonable to assume that the lithosphere is close to a thermal steady state. For a lithosphere, with constant heat production and thermal conductivity layers, the temperatures as a function of depth within each layer can be solved by bootstrapping from the surface with known surface temperature, T_0, and surface heat flow, q_0:

$$T(z_i < z \leq z_{i+1}) = T_i + (q_i/k_{i+1})\,(z - z_i) - (A_{i+1}/2k_{i+1})\,(z - z_i)^2 \quad , \tag{2}$$

where k_{i+1} and A_{i+1} are conductivity and heat production in the layer, respectively. The temperature T_i is determined by the temperature at the base of the previous layer, $T(z_i)$ and heat flow at the top of each layer q_i is determined by subtracting the radiogenic heat flow from the layer above, i.e., $q_i = q_{i\text{-}1} - A_i(z_i - z_{i\text{-}1})$. The initial thermal gradient depends q_0/k_1, while heat production governs geotherm curvature. As discussed above, thermal conductivity is reasonably constrained, while heat production can vary over an order or two in magnitude and variations in deeper heat flow by a factor 5-10.

For several different end-member controls, **Fig. 9** illustrates the ranges of lithospheric temperatures expected given observed ranges of surface heat flow, crustal heat production, mantle heat production and conductivity. For these example geotherms, the lithosphere was represented by three layers: an upper crust of 12 km, a lower crust of 24 km and a mantle lithosphere, each with constant amounts of heat production. Lower crustal heat production, A_{LC}, is set to 0.4 μW m^{-3} in all cases, while

two end-member values of mantle heat production, A_m, of 0 and 0.06 μW m^{-3} are evaluated. Crustal and mantle thermal conductivity are set to 2.7 and 3.0 W m^{-1} K^{-1}, respectively. The range of steady-state shapes that can be achieved is limited, and shapes can be characterised by Moho temperature, T_M, Moho heat flow, q_M, and thickness of the thermal lithosphere, L_T, which we define as the depth where the steady-state conductive geotherm intersects the mantle adiabat. **Fig. 10** shows these parameters for the geotherm families in **Fig. 9**.

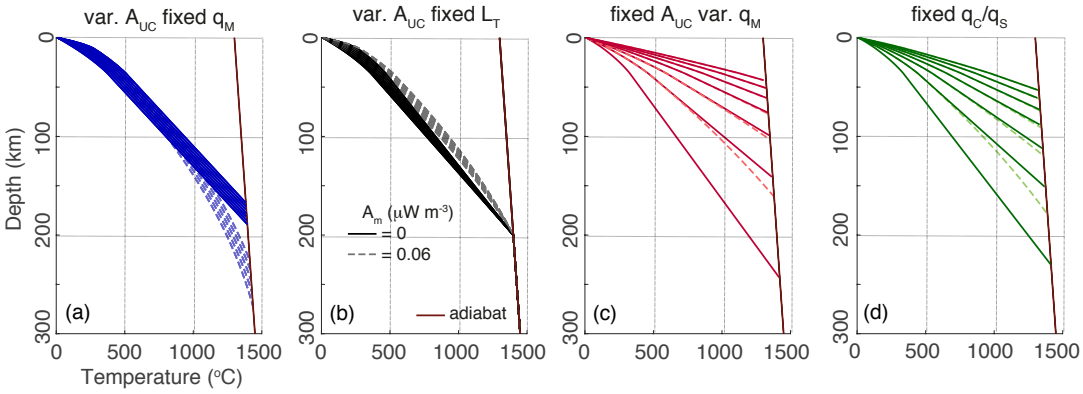

Fig. 9. *Illustration of the geotherm ranges for different geotherm families. On each panel, the geotherms are for the same values of q_S (from 35 and 95 mW m^{-2}, every 10 mW m^{-2}). Crustal thickness is assumed to be a constant 36 km, with a 12 km upper crust; A_{LC} is constant at 0.4 μW m^{-3} Solid coloured lines are for A_m=0, lighter coloured dashed lines for A_m = 0.06 μW m^{-3}. (a) Constant Moho heat flow geotherms, q_M = 20 mW m^{-2}. (b) Same crustal heat production as (a), but for fixed L_T=200 km. (c) Constant crustal heat production, A_{UC} =3 A_{LC} (d) Coupled heat flow-heat production geotherms following Hasterok and Chapman [2011], i.e. heat flow at the base of the upper crust q_C= 0.75·q_S. Note that geotherms for q_S=35 mW m^{-2} and A_m =0.06 μW m^{-3} in panel c and d are not shown, because, due to their curvature, they never intersect or approach the mantle adiabat (brown).*

Lithospheric temperatures would only span a narrow range if crustal heat production variations exerted the main control on thermal structure (**Fig. 9**a,b), and a very large range of A_{UC} would be required (**Fig. 10**). This is true irrespective of whether a fixed Moho heat flow (**Fig. 9**a) or a fixed lithospheric thickness (**Fig. 9**b) is assumed to represent the effects of dynamic lithosphere-mantle interaction. To match the large lithospheric temperature range inferred from xenoliths and geophysical observations (Section 2), heat flow at the Moho needs to vary by at least a factor 3 to 4 globally (**Fig. 10**), either independently of (**Fig. 9**c) or in conjunction with crustal heat production (**Fig. 9**d) [*Hasterok and Chapman*, 2011]. The correlation between heat production and heat flow from larger depths is usually parameterized as a constant ratio between surface heat flow, q_S, and heat flow at the base of the upper crust, q_C. Note that for such a geotherm family, the heat flow at the base of the Moho, i.e. below most of the heat production, is a decreasing fraction of q_S with increasing q_S (**Fig. 10**b,e).

Moho temperature is strongly correlated with Moho heat flow (**Fig. 10**b,c), as expected from comparing the expressions for temperature at the base of a layer, T_H =

$T_0 + (q_0 - AH/2) \cdot H/k$ and heat flow at the base of the layer, $q_H = (q_0 - AH)$, where H is the layer's thickness. While basal heat flow only depends on the integrated heat production in the layer, basal temperatures are also affected by how heat production varies with depth in the layer. A stronger concentration of heat production towards the surface leads to a stronger curvature of the geotherm, and for the same q_H, a lower T_H. I.e., higher upper than lower crustal heat production leads to lower Moho temperature for the same total crustal heat production. The effect amounts to about 100 degrees for $A_{UC} = 4 \cdot A_{LC}$ compared to $A_{UC} = A_{LC}$. While for petrological applications such a temperature difference can be significant and it may be sufficient to affect lithospheric viscosity and thereby lithospheric evolution [*Sandiford and McLaren*, 2002], for the resolution of many geophysical observations, this is a modest effect compared to the variation in q_M and T_M in response to variations in surface heat flow and integrated crustal heat production.

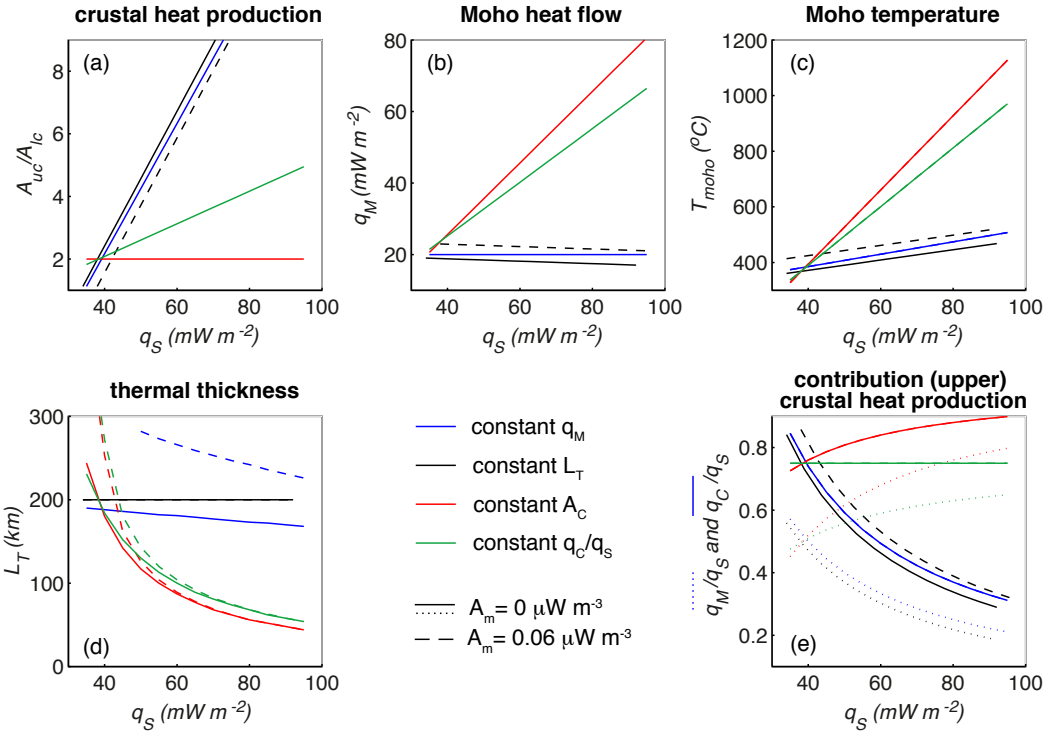

Fig. 10. *Variations in steady-state geotherm characteristics with thermal parameters for the sets of geotherms in Fig. 9, i.e. thermal differences solely controlled by variations in crustal heat production, A_C (through variations in upper crustal heat production) with either Moho heat flow, q_M, or thermal thickness of the conductive lithosphere, L_T, fixed, or thermal differences controlled solely by varying Moho heat flow, or as a correlated variation in upper crustal heat production and heat flow that enters the base of the upper crust, q_C. Solid and dashed lines are for two different values of heat production A_m in the mantle lithosphere.*

For cases where q_M variations exert a dominant control on q_S, thermal lithospheric thickness is strongly related to Moho heat flow (compare **Fig. 10**d and b). For lithosphere exceeding about 150 km thickness, heat production in the mantle lithosphere can play a significant role in curving the geotherm if heat production is towards the higher end of the observed range (**Fig. 9**, **Fig. 10**). For thinner lithosphere, the integrated effect of mantle heat production is small and can be neglected. With a reasonable amount of crustal heat production (average of 0.5 μW m^{-}

^{3} or higher) steady state thermal lithosphere tends to be > 50 km in thickness (**Fig. 10**). Although for old lithosphere it has been inferred that Moho heat flow does not vary much, a range of 10 to 20 mW m^{-2} (which includes uncertainties) [*Jaupart and Mareschal*, 2014] actually corresponds to a variation in lithospheric thickness from over 350 to 200 km, i.e. in this sense, 10 to 20 mW m^{-2} is a wide range of Moho heat flow values.

Coupled heat flow-heat production family like the one shown in **Fig. 9**d have commonly been used as reference model to characterise continental lithospheric temperatures. A range of studies estimated scaling factors between integrated upper crustal heat production and surface heat flow and found preferred values of 0.25 to 0.4 [*Pollack and Chapman*, 1977; *Artemieva and Mooney*, 2001; *Hasterok and Chapman*, 2011]. Such values require that upper crustal heat production is at least a factor of 2 to 3 higher than heat production in the lower crust or else such scaled models would only be compatible with a limited range of surface heat flow values for the estimated range of average crustal heat production. This range of relative upper to lower crustal heat production is consistent with constraints from heat production observations (Section 3.3). Below (Section 4.2), we discuss how applicable such a model is.

4.2. Numerical steady state geotherms

What is not captured by the analytical models of the previous section is that in numerical models where a higher-viscosity lithosphere overlies a lower-viscosity convective mantle, there is a transitional layer between the dominantly conductive lithosphere and the dominantly convective mantle which can participate in small-scale convection and where thermal structure can in fact be hotter or cooler than the steady-state average over length scales of a few 100 km and time scales of several million years [*Davaille and Jaupart*, 1994; *Doin et al.*, 1997; *Cooper et al.*, 2004]. As a result of the inherent convective instability of the base of thick cold lithosphere, there is an upper limit to lithospheric thickness. Several numerical studies indicate that with plausible lithospheric rheology, lithosphere without additional compositional stabilisation reaches a maximum effective thermal thickness (defined as the intersection of the best fitting steady-state 1-D geotherm and the adiabat) of about 150 km [*Cooper et al.*, 2004; *Wang et al.*, 2014](**Fig. 11**). Compositional strengthening, possibly aided by compositional buoyancy, can stabilize lithosphere to larger depths [*Doin et al.*, 1997; *Wang et al.*, 2014]. Xenoliths indicate chemical thicknesses of up to 170 to 220 km [e.g. *O'Reilly and Griffin*, 2010]. Such chemical thicknesses could explain lithospheric temperatures that remain below the mantle adiabat down to depths up to about 300 km.

Fig. 11 shows how the analytical geotherms from the previous section compared with averaged geotherms for several numerical cases from *Cooper et al.* [2004], where temperatures in the conductive part of the lithosphere have reached a steady-state. They model the temperatures for a system consisting of a rigid 2-layer crust with different amounts of upper vs. lower crust heat production [*Cooper et al.*, 2004] overlying a mantle with a strongly temperature-dependent viscosity. This leads to the

formation of a thick conductive thermal boundary layer stabilised by high viscosity. In some cases, they assume an additional chemically stabilised lithospheric root over part of their domain.

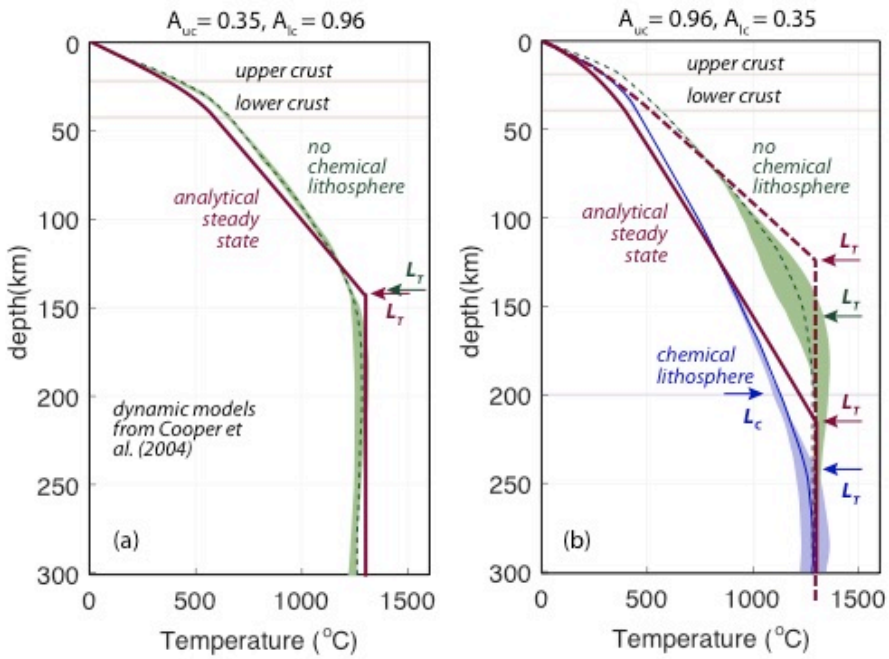

Fig. 11. *Comparison of analytical 1-D steady state geotherms (red lines), and geotherms predicted by numerical models from [Cooper et al., 2004] (green and blue lines and shading) where a rigid two layer crust with different amounts of upper and lower crustal heat production, A_{UC} and A_{LC}, overlies a mantle with strongly temperature dependent viscosity which leads to the formation of a thick thermal boundary layer. Solid red lines are analytical solutions assuming q_S is known, dashed red line is a solution assuming L_T is known. Numerical geotherms shown are the average (lines) and range (shading) for when the models essentially reach a steady state in the conductive lithosphere. The range is due to thermal fluctuations in the transient and convective mantle.*

Cases like the one shown in panel (a), with $A_{LC} > A_{UC}$ and without a chemical root, lead to relatively warm and thin lithosphere and are well modelled by 1-D steady-state analytical geotherms constrained by a surface heat flow corresponding to that observed in the models. In this case, the transient layer only slightly modulates the geotherm through time. However, for cases like the green case in panel (b), with the same integrated heat production, but this time more concentrated in the upper crust, and again without a chemical root, the lower lithospheric temperatures lead to a denser, more convectively unstable lithosphere with a thicker transient layer at its base. The result is an effective thermal thickness that is 50-100 km smaller and a Moho temperature that is 100-200°C higher than that predicted by the same type of analytical solution that imposes q_S and the known A_{UC}, A_{LC}. Case (b) is better approximated by an analytical geotherm with a prescribed lithospheric thickness (dashed case in panel b). If part of the thermal boundary layer is chemically stabilised as in the blue geotherm in case b, then the prediction of temperatures from surface heat flow is again a reasonable approximation. Hence predicting geotherms from just observed surface heat flow and estimated crustal heat production may lead to quite

wrong estimates of lithospheric temperatures. Information on thermal thickness (e.g. from seismic measures), or temperatures at another depth in the lithosphere (e.g. from magnetic measurements, and/or from seismic or magnetotelluric constraints) can help improve the estimates of lithospheric geotherms.

It has been suggested that the depth where a temperature of around 1100°C is reached is a better measure of thermal thickness, as it more closely represents the depth above which heat transport is purely conductive [*Afonso et al.*, 2008]. However, seismically, we have the best chance of imaging the velocity minimum that occurs near the intersection of the lithospheric geotherm and the mantle adiabat, and our definition of L_T is closer to this seismic measure, although it may still be an underestimate by up to a few tens of km.

4.3. Heat-flow based geotherm families

Pollack and Chapman [1977] were the first to formulate a continental geotherm family comprising steady-state 1-D geotherms as a function of surface heat flow. Previous studies [*Polyak and Smirnov*, 1968; *Roy et al.*, 1968; *Lachenbruch*, 1970] had noted that there is a broad correlation between tectonic age of the continents and heat flow (**Fig. 3**), as well as correlations between surface heat flow and crustal heat production (**Fig. 7**). *Pollack and Chapman* [1977] used the data to estimate that 40% of surface heat flow is generated within the upper continental crust and 60% is derived from heat production in the lower crust and mantle lithosphere and from the convecting mantle below. They assumed constant heat production in the lower crust and mantle, so their parameterization implies that heat flow from the convecting mantle into the base of the upper crust (residual heat flow q_C) covaries with surface heat flow. As mantle heat production is low, the Pollack and Chapman geotherm family is one where crustal heat production and lithospheric thickness vary together. This might imply that crustal heat production exerts an important control on lithospheric keel preservation and/or lithospheric cooling [*Sandiford and McLaren*, 2002; *Cooper et al.*, 2004; *Jaupart and Mareschal*, 2014]

These sets of geotherms have for the past 40 years served as reference for the thermal structure of continental lithosphere. Recent studies based on expanded data sets and complemented by additional constraints, estimate the upper crust contributes between 25 and 35% to surface heat production [*Artemieva and Mooney*, 2001; *Hasterok and Chapman*, 2011] (**Fig. 9**d). It has also been confirmed that the thermal structure from such geotherms is consistent with both the range of seismic velocities in the continental lithosphere and variations in seismic thickness of the lithosphere [e.g. *Goes et al.*, 2000; *Röhm et al.*, 2000; *Goes and Van der Lee*, 2002; *Godey et al.*, 2004; *Shapiro and Ritzwoller*, 2004a; *Dalton and Faul*, 2010] as well as with topography as predicted from isostasy [*Hasterok and Chapman*, 2007; *Hasterok and Chapman*, 2011; *Hasterok and Gard*, 2016]. Furthermore, xenolith-derived geotherms span a similar temperature range [*Rudnick et al.*, 1998; *O'Reilly and Griffin*, 2006].

Upon more careful examination, it is however clear that a correlation between surface heat flow and crustal heat production and tectonic age is only a very first-

order global trend that emerges when broad time intervals (Phanerozoic, Precambrian, Archean) or global ranges are considered [*Jaupart and Mareschal*, 2007; 2014]. On a regional scale, in particular in Paleozoic and older provinces, much of the variation in surface heat flow appears to be due to variable crustal heat production without accompanying variations in mantle heat flow [*Jaupart and Mareschal*, 2007]. Dynamic models confirm that stable continents tend to evolve to a steady state where the variations in heat flow at the Moho are subdued (within ~10 mW m^{-2}) compared to the variations due to variable crustal heat production (which can contribute up to 30-40 mW m^{-2}) [*Cooper et al.*, 2004].

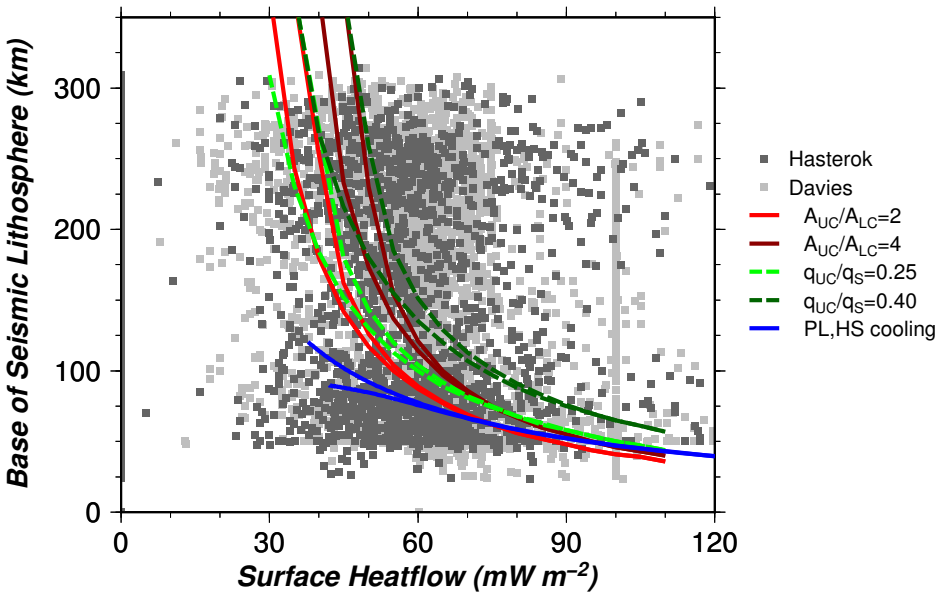

Fig. 12. *Seismic lithospheric thickness (LITH1.0) vs. continental surface heat flow (from current global heat flow data base updated from Hasterok and Chapman [2011] in dark gray symbols, and Davies [2013] light gray symbols). Lines show predicted trends for a range of thermal models for oceanic half-space (HS) and plate cooling (PL) (in bright blue, with smallest thicknesses for the plate model) and steady-state continental geotherms (other colours). For the continental models, light green lines assume upper crustal heat production A_{UC}, contributes a constant fraction of 25% to surface heat flow, dark green lines a constant fraction of 40%. Red and dark red lines assume a constant ratio of upper/lower crustal heat production with A_{UC}=2 times and 4 times A_{LC}, respectively, and A_{LC}=0.4 μW m^{-3}. For the continental models, the lowest heat flow curve is for A_m= 0 and the highest for A_m = 0.06 μW m^{-3}. A large variation in seismic thicknesses as a function of surface heat flow is found and would require a range of contributions in crustal heat production rather than a single correlation.*

However, over continents of all ages, Moho heat flow needs to vary substantially, spanning a range from about 10 to at least 70 mW m^{-2}, although these variations do not need to be coupled to crustal heat production [*Hasterok and Gard*, 2016] (**Fig. 9**c,d). Indeed, also for higher heat flow regions, it is rather unlikely that Moho heat flow and heat production increase together with a close to constant scaling factor. In the best constrained compilations, heat production does increase somewhat with decreasing tectonic age [*Jaupart and Mareschal*, 2014; *Gard et al.*, 2019b; *Hasterok et al.*, 2019](**Fig. 3**), but not rapid enough to account for the increase in heat flow and decrease in thermal thickness of the lithosphere. So, although practical as a reference,

the coupled heat flow-heat production thermal models do not actually reflect what controls the thermal state of the continental lithosphere.

In these continental geotherm families, like in oceanic lithosphere, variations in thermal lithospheric thickness and consequent variations in Moho heat flow exert the main control on the variation in the temperatures in the mantle part of the continental lithosphere. Variations in crustal heat production can significantly influence surface heat flow, and in a dynamic setting, different amounts and differentiation of heat production in the crust leads to some amount of thermal blanketing, which may influence Moho heat flow. A significant control of lithospheric thickness, and thereby Moho heat flow, on surface heat flow is consistent with the distribution of continental seismic lithospheric thickness vs surface heat flow data (**Fig. 12**). The data form quite a scattered cloud, but steady-state continental trends for constant heat production do overlay the thick-lithosphere part of cloud, while the thin lithosphere-low heat flow points are more like what might be expected from oceanic cooling models.

4.4. Geophysically based estimates of crustal heat production below US

Seismic thicknesses have limited depth resolution and may not only reflect thermal thickness. Other data may allow better constraints on thermal structure of the lithosphere. Below, we show an example that uses the results from a recent study that constrained Moho temperatures below much of the US by mapping Pn velocities into lithospheric temperatures [*Schutt et al.*, 2018]. The depth of the Curie temperature [e.g. *Bouligand et al.*, 2009] could be used in a similar a manner, although this gives a measure of temperature within the crust so would provide less constraint on total crustal heat production.

The Pn model used by *Schutt et al.* [2018] has Moho depths less than 30 km in areas of Cenozoic extension, i.e., the Basin and Range and northern Mexico, as well as along the subduction influenced western US coast (**Fig. 13**b). High Moho temperatures, exceeding 700°C, were found over a larger region, including the extinct and current arcs, the Snake River Plain and Yellowstone, parts of the Basin and Range and the Rio Grande Rift, as well as the northern part of the Great Plains near the Canadian border **Fig. 13**c). The high Moho temperature regions are also generally characterised by high surface heat flow, exceeding 65 mW m^{-2} (**Fig. 13**a). We model these three sets of observations (surface heat flow, Moho depth and Moho temperature) with 1-D steady-state geotherms assuming: (i) constant crustal heat production in two layers, with upper crustal heat production equal to 3 times lower crustal heat production, (ii) a lower crust twice as thick as the upper crust. (iii) a constant value of crustal thermal conductivity =2.5 W K^{-1} m^{-1}. The resulting Moho heat flow, upper crustal heat production and the ratio of heat flow from heat produced in the upper crust ($q_{UC}=A_{UC}H_{UC}$) over total surface heat flow (q_S) are shown in **Fig. 13**d, e, and f, respectively.

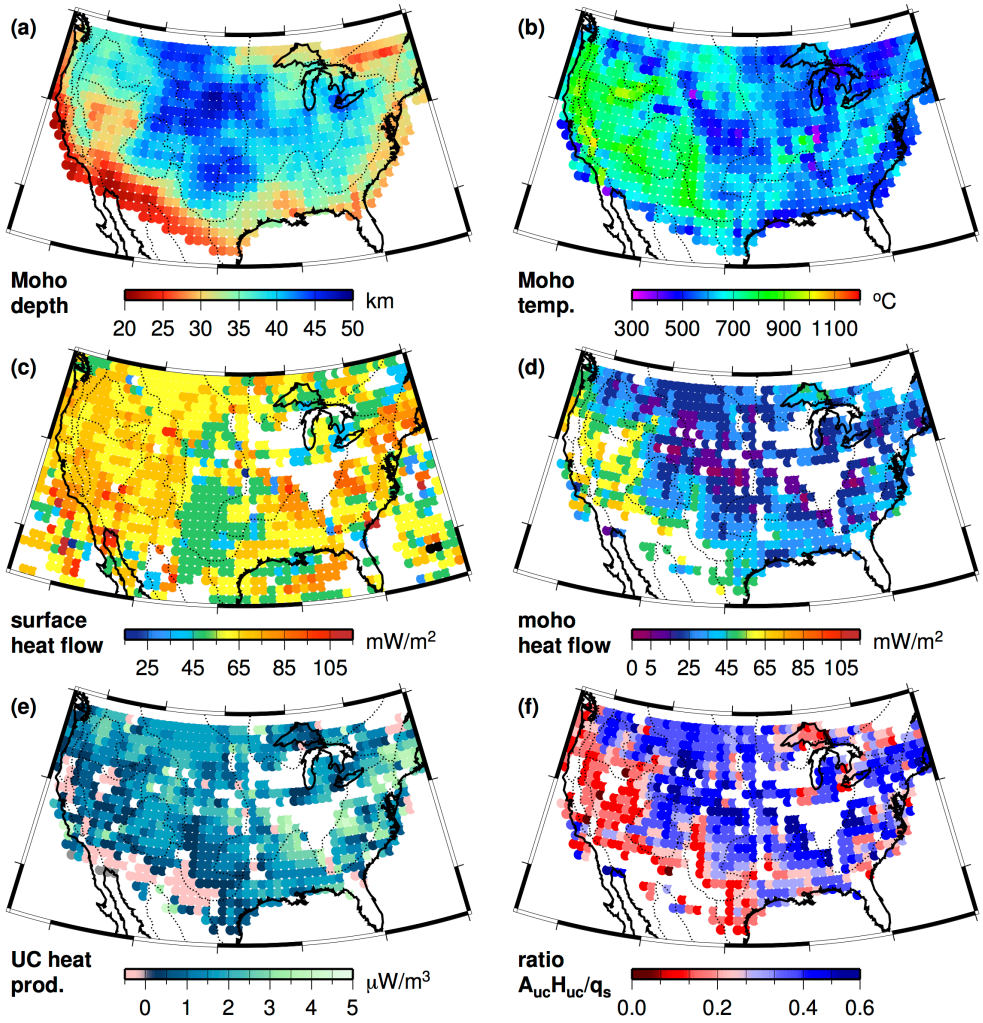

Fig. 13. *Moho depth (a) and temperature (b), both smoothed from Schutt et al. 2018, and surface heat flow (c, global heat flow data base, smoothed over 100 km radial caps) are used to estimate Moho heat flow (d), crustal heat production (e), and the ratio of heat flow generated in the upper crust (i.e. integrated upper crustal heat production $A_{UC}H_{UC}$) over surface heat flow (f). The modelling assumes steady-state geotherms, with an upper crust 1/3 of crustal thickness, and a constant ratio of upper to lower crustal heat production of 3. Pink areas in panel (e) represent regions where Moho temperature exceeds the temperature that could be explained purely by conduction without heat production by more than 50°C.*

There are a number of things to note about these results:

(1) Surface heat flow is likely affected by advective processes in a number of locations. In particular, some of the lowest heat flow values in the central US are too low to be explained by normal steady-state models, and in various places in the western US, magmatic transport and fluid flow likely bias heat flow values either high or low.

(2) The results shown in **Fig. 13** are for constant A_{UC}/A_{LC}=3, but are similar if this ratio is set to 2 or 4, and also if the ratio of the thickness of upper and lower crust is varied.

(3) Certainly not the whole region is expected to be in a thermal steady state, but we map "apparent" crustal heat production. For part of the western US (in particular where the crust is very thin), the Moho temperatures are too high to allow any

contribution of crustal heat production (pink areas in panel e). These are areas where *Schutt et al.* [2018] propose a contribution of melt to the low Pn velocities.
(4) Indeed, *Bouligand et al.* [2009] inferred very shallow Curie temperature depths, of less than 5-10 km, below substantial parts of the Basin and Range, below the Snake River Plain and Rio Grande Rift. Such depths are too shallow for any steady-state geotherm and would require significant advective heat transfer (e.g. by magma). Where defined, our q_S-T_M constrained geotherms predict Curie temperature depths of 20-30 km for the study region of *Bouligand et al.* [2009] which is within the range of their estimates away from these shallow Curie depth areas.
(4) We cannot model the Moho temperatures with a constant heat partitioning (constant $q_{UC}/q_S = A_{UC}H_{UC}/qs$) model. In the stable (eastern) parts of the continent, we require that upper crustal heat production contributes a larger part of surface heat flow than the 25-40% in global geotherm families, while in the active western US the apparent contribution of crustal heat production is mostly lower than this.
(5) A higher contribution of (upper) crustal heat production to the surface heat flow is consistent with studies in stable cratons where good constraints on heat production are available [*Perry et al.*, 2006; *Jaupart and Mareschal*, 2007]. Such studies estimate Moho heat flow of around 15 mW m^{-2}, for surface heat flow in the range of 45-55 mW m^{-2}. With a lower crust of around 25 km thick and 0.4 μW m^{-3}, this yields a contribution of upper crustal heat production of 45-55%.
(6) The lower apparent contribution of (upper) crustal heat production to areas of recent tectonic activity may in part reflect a non-steady thermal state. Note that tectonic processes that lead to rapid crustal stretching or to crustal thickening tend to produce geotherms with an increased downward curvature at crustal depths (see Supplement), i.e. high apparent crustal heat production. A low apparent heat production (low curvature) could be due to heating the lithosphere from below (see Supplement). The high (near dry solidus) temperatures at the base of the lithosphere below the Basin and Range inferred from petrology may also point to such heating from below.

This analysis, although subject to considerable uncertainties, does illustrate what might be possible with better constraints. Together with the seismic thickness discussion in Section 4.2, this points to a constant A_{UC}/A_{LC} model as possibly a better first order representation than the constant q_{UC}/q_S models often used, although it needs to be borne in mind that also A_{UC}/A_{LC} has been found to vary considerably where data is available [e.g. *McLaren et al.*, 2003; *Perry et al.*, 2006].

5. Conclusions

Surface heat flow, the petrology from crust and mantle samples, seismic, magnetic and electromagnetic observations together provide considerable constraints on the thermal structure of continental lithosphere. Steady-state one-dimensional geotherms provide a useful description of thermal structure for large parts of the continental lithosphere even if not all of it is in an actual steady state. Commonly used families of

geotherms assume that crustal heat production and surface heat flow are correlated according to an average global trend. However, where more detailed constraints are available it is clear that these two are not usually correlated. The range of lithospheric temperatures from xenotherms and seismic constraints requires that, on average, about 50% of surface heat flow is controlled by heat advected from mantle (reflected in thermal lithospheric thickness). The rest of the heat is derived from crustal heat production, where (in general) upper-crustal heat production is 2-4 times higher than that in the lower crust, consistent with its more felsic composition. Pn-derived Moho temperature estimates for the US indicate that for the stable continental core in the east, upper-crustal heat production is the source of around 50% of the surface heat flow, while for the thin thermal lithosphere in the tectonically active western US the contribution from upper-crustal heat production is generally less than 20% and there are several regions where the presence of melt probably contributes to low Pn velocities. To further constrain heat sources and thermal structure, seismic observations provide the most widespread and detailed information, where possible combined with other constraints such as xenotherms, composition from xenoliths, magnetic field, magnetotellurics, and gravity.

Acknowledgments This work was initiated at a CIDER funded (NSF EAR-1135452) workshop held in Fort Collins, May 2017. We thank two reviewers for their supportive comments. SG thanks Thomas Eeken, Emily White and Suzan van der Lee for discussions. This research was supported partially by the Australian Government through the Australian Research Council's Discovery Projects funding scheme (project DP180104074) to DH, partially by National Science Foundation grant EAR-1358664 to DS.

References

Adam, C., and V. Vidal (2010), Mantle Flow Drives the Subsidence of Oceanic Plates, *Science*, *328*, 83-85.

Afonso, J. C., G. Ranalli, and M. Fernandez (2007), Density structure and buoyancy of the oceanic lithosphere revisited, *Geophys. Res. Lett.*, *34*, L10302, doi: 10310.11029/12007GL029515.

Afonso, J. C., M. Moorkamp, and J. Fullea (2016a), Imaging the Lithosphere and Upper Mantle: Where We Are At and Where We Are Going, in *Integrated Imaging of the Earth: Theory and Applications, Geophysical Monograph 218*, edited by M. Moorkamp, P. G. Lelièvre, N. Linde and A. Khan, pp. 191-218, Am. Geophys. Un., John Wiley & Sons, Hoboken.

Afonso, J. C., M. Fernandez, G. Ranalli, W. L. Griffin, and J. A. D. Connolly (2008), Integrated geophysical-petrological modeling of the lithosphere and sublithospheric upper mantle: methodology and applications, *Geochem. Geophys. Geosystems*, *9*, Q05008.

Afonso, J. C., J. Fullea, Y. Yang, J. A. D. Connolly, and A. G. Jones (2013a), 3-D multiobservable probabilistic inversion for the compositional and thermal structure of the lithosphere and upper mantle. II: General methodology and resolution analysis, *J. Geophys. Res.*, *118*, 1650-1676.

Afonso, J. C., J. Fullea, W. L. Griffin, Y. Yang, A. G. Jones, J. A. D. Connolly, and S. Y. O'Reilly (2013b), 3-D multiobservable probabilistic inversion for the compositional and thermal structure of the lithosphere and upper mantle. I: a priori petrological information and geophysical observables, *J. Geophys. Res.*, *118*, 2586-2617.

Afonso, J. C., N. Rawlinson, Y. Yang, D. L. Schutt, A. G. Jones, J. Fullea, and W. L. Griffin (2016b), 3-D multiobservable probabilistic inversion for the compositional and thermal structure of the lithosphere and upper mantle: III. Thermochemicaltomography in the Western-Central U.S., *J. Geophys. Res.*, *121*, 7337–7370.

Alessio, K. L., M. Hand, D. E. Kelsey, M. A. Williams, L. J. Morrissey, and K. Barovich (2018), Coservation of deep crustal heat production, *Geology*, *46*(4), 335-338.

An, M., D. A. Wiens, Y. Zhao, M. Feng, A. A. Nyblade, M. Kanao, Y. Li, A. Maggi, and J.-J. Lévêque (2015), S-velocity model and inferred Moho topography beneath the Antarctic Plate from Rayleigh waves., *J. Geophys. Res.*, *120*, 359-383.

Anderson, D. L. (1995), Lithosphere, asthenosphere, and perisphere, *Rev. Geophys.*, *33*(1), 125-149.

Andreoli, M. A., R. J. Hart, L. D. Ashwal, and H. Coetzee (2006), Correlations between U, Th content and metamorphic grade in the western Namaqualand Belt, South Africa, with implications for radioactive heating of the crust, *J. Petrol.*, *47*, 1095-1118.

Artemieva, I. (2006), Global 1º × 1º thermal model TC1 for the continental lithosphere: implications for lithosphere secular evolution, *Tectonophysics*, *416*, 245-277.

Artemieva, I. M., and W. D. Mooney (2001), Thermal thickness and evolution of Precambrian lithosphere: a global study, *J. Geophys. Res.*, *106*(8), 16,387-316,414.

Artemieva, I. M., H. Thybo, K. Jakobsen, N. K. Sørensen, and L. S. K. Nielsen (2017), Heat production in granitic rocks: Global analysis based on a new data compilation GRANITE2017, *Earth Sci. Rev.*, *172*(1-26).

Beghein, C., Z. Xing, and S. Goes (2019), Thermal Nature and Resolution of the Lithosphere-Asthenosphere Boundary Under the Pacific From Surface Waves, *Geophys. J. Int.*, *2*, 1441-1465.

Beghein, C., K. Yuan, N. Schmerr, and Z. Xing (2014), Changes in Seismic Anisotropy Shed Light on the Nature of the Gutenberg Discontinuity, *Science*, *343*, 1237-1240.

Behn, M. D., and P. B. Kelemen (2003), Relationship between seismic P-wave velocity and the composition of anhydrous igneous and meta-igneous rocks, *Geochem. Geophys. Geosys.*, *4*(5), 1041.

Bell, D. R., M. D. Schmitz, and P. E. Janney (2003), Mesozoic thermal evolution of the southern African mantle lithosphere., *Lithos*, *71*, 273–287.

Bijwaard, H., W. Spakman, and E. R. Engdahl (1998), Closing the gap between regional and global travel time tomography, *J. Geophys. Res.*, *103*, 30,055-030,078.

Blackwell, D. D., and M. Thakur (2007), Birch's Crustal Heat Production-Heat Flow Law: Key to Quantifying Mantle Heat Flow as a function of time., *Eos Trans. AGU Fall Meeting Suppl.*, *88*(52), T22B-07.

Bouligand, C., J. M. Glen, and R. J. Blakely (2009), Mapping Curie temperature depth in the western United States with a fractal model for crustal magnetization, *J. Geophys. Res.*, *114*, B11104.

Boyd, F. R. (1973), A pyroxene geotherm., *Geochim Cosmochim Acta*, *37*, 2533–2538.

Brey, G., and T. Köhler (1990), Geothermobarometry in four-phase Lherzolites II. New thermobarometers, and practical assessment of existing thermobarometers. , *J. Petrol.*, *31*, 1353–1378.

Brown, E. L., and C. E. Lesher (2016), REEBOX PRO: A forward model simulating melting of thermally and lithologically variable upwelling mantle, *Geochem. Geophys. Geosys.*, *17*(10), 3929-3968.

Bussweiler, Y., G. Brey, D. G. Pearson, T. Stachel, R. A. Stern, M. F. Hardman, B. A. Kjarsgaard, and S. E. Jackson (2017), The aluminum-in-olivine thermometer for mantle peridotites — Experimental versus empirical calibration and potential applications, *Lithos*, *272–273*, 301-314.

Canil, D., and H. S. C. O'Neill (1996), Distribution of Ferric Iron in some Upper-Mantle Assemblages, *J. Petrol.*, *37*(3), 609–635.

Carlson, R. W., D. G. Pearson, and D. E. James (2005), Physical, chemical and chronological characteristics of continental mantle, *Rev. Geophys.*, *43*, RG1001.

Carson, C. J., S. McLaren, J. L. Roberts, S. D. Boger, and D. D. Blankenship (2013), Hot rocks in a cold place: high sub-glacial heat flow in East Antarctica, *J. Geol. Soc. London*, *171*, 9012.

Chapman, D. S. (1986), Thermal gradients in the continental crust, in *The Nature of the Lower Continental Crust*, edited by J. B. Dawson, D. A. Carswell, J. Hall and K. H. Wedepohl, pp. 63-70, Geol. Soc. London, London, U.K.

Chiozzi, P., V. Paquale, M. Verdoya, and P. D. Felice (2000), Practical applicability of field upgamma-ray scintillation spectrometry in geophysical surveys., *Applied Radiation and Isotopes*, *53*, 215-220.

Chopping, R., and B. L. N. Kennett (2015), Maximum depth of megnetisation of Australia, its uncertainty, and implications for Curie depth, *Geo. Res. J.*, *7*, 70-77.

Cooper, C. M., A. Lenardic, and L. Moresi (2004), The thermal structure of stable continental lithosphere within a dynamic mantle, *Earth Planet. Sci. Lett*, *222*, 807-817.

Dalton, C. A., and U. H. Faul (2010), The oceanic and cratonic upper mantle: Clues from joint interpretation of global velocity and attenuation models, *Lithos*, *120*, 160-172.

Dalton, C. A., X. Bao, and Z. Ma (2017), The thermal structure of cratonic lithosphere from global Rayleigh wave attenuation, *Earth Planet Sci. Lett.*, *457*, 250-262.

Davaille, A., and C. Jaupart (1994), Onset of thermal convection in fluids with temperature-dependent viscosity: Application to the oceanic mantle *J. Geophys. Res.*, *99*(B10), 19,853-866.

Davies, J. H. (2013), Global map of solid Earth surface heat flow, *Geochem. Geophys. Geosys.*, *14*(10), 4608-4622.

Davies, J. H., and D. R. Davies (2010), Earth's surface heat flux, *Solid Earth*, *1*, 5-24.

Deen, T. J., W. L. Griffin, G. Begg, S. Y. O'Reilly, L. M. Natapov, and J. Hronsky (2006), Thermal and compositional structure of the subcontinental lithospheric mantle: Derivation from shear wave seismic tomography, *Geochem. Geophys. Geosys.*, *7*(7), Q07003.

Doin, M. P., L. Fleitout, and U. R. Christensen (1997), Mantle convection and stability of depleted and undepleted continental lithosphere, *J. Geophys. Res.*, *102*(B2), 2771-2787.

Dye, S. T. (2012), Geoneutrinos and the radioactive power of the Earth, *Rev. Geophys.*, *50*, RG3007.

Eaton, D. W., F. Darbyshire, R. L. Evans, H. Grütter, A. G. Jones, and X. Yuan (2009), The elusive lithosphere–asthenosphere boundary (LAB) beneath cratons, *Lithos*, *109*, 1-22.

Eeken, T., S. Goes, H. A. Pedersen, N. T. Arndt, and P. Bouilhol (2018), Seismic evidence for depth-dependent metasomatism in cratons., *Earth Planet Sci. Lett.*, *491*, 148-159.

Finnerty, A. A., and F. R. Boyd (1987), Thermobarometry for garnet peridotites: Basis for the determination of thermal and compositional structure of the upper mantle, in *Mantle Xenoliths*, edited by P. H. Nixon, pp. 381–402, John Wiley, Hoboken, N. J.

Fischer, K. M., H. A. Ford, D. L. Abt, and C. A. Rychert (2010), The Lithosphere-Asthenosphere Boundary, *Annu. Rev. Earth Planet. Sci.*, *38*, 551-575.

Flück, P., R. D. Hyndman, and C. Lowe (2003), Effective elastic thickness Te of the lithosphere in western Canada, *J. Geophys. Res.*, *108*(B9).

Garber, J. M., et al. (2018), Multidisciplinary Constraints on the Abundance of Diamond and Eclogite in the Cratonic Lithosphere, *Geochem. Geophys. Geosys.*, *19*(7), 2062-2086.

Gard, M., D. Hasterok, and J. Halpin (2019a), Global whole-rock geochemical database compilation, *Earth System Sci. Data*, *11*, 1553–1566

Gard, M., D. Hasterok, M. Hand, and G. Cox (2019b), Variations in continental heat production from 4 Ga to the present: Evidence from geochemical data, *Lithos*, *342-343*, 391-406.

Garel, F., Thoraval, C., 2020. Chasing the transition from lithosphere to asthenosphere in thermo-mechanical models of mantle and plate dynamics. *Phys. Earth Planet. Int.* Special Issue LIthosphere-Asthenosphere, in review.

Ghiorso, M., M. Hirschmann, P. Reiners, and V. Kress (2002), The pMELTS: A revision of MELTS for improved calculation of phase relations and major element partitioning related to partial melting of the mantle to 3 GPa, *Geochem. Geophys. Geosys.*, *3*(5), 1-35.

Godey, S., F. Deschamps, J. Trampert, and R. Snieder (2004), Thermal and compositional anomalies beneath the North American continent, *J. Geophys. Res.*, *109*, B01308, doi: 01310.01029/02002JB002263.
Goes, S., and S. Van der Lee (2002), Thermal structure of the North American uppermost mantle inferred from seismic tomography, *J. Geophys. Res.*, *107*(B3), 2000JB000049.
Goes, S., R. Govers, and P. Vacher (2000), Shallow upper mantle temperatures under Europe from *P* and *S* wave tomography, *J. Geophys. Res.*, *105*, 11,153-111,169.
Goes, S., F. J. Simons, and K. Yoshizawa (2005), Seismic constraints on temperature of the Australian uppermost mantle, *Earth Planet. Sci. Lett*, *236*, 227-237.
Goes, S., C. M. Eakin, and J. Ritsema (2013), Lithospheric cooling trends and deviations in oceanic PP-P and SS-S differential traveltimes, *J. Geophys. Res.*, *118*, 1-12.
Goes, S., J. Armitage, N. Harmon, H. E. Smith, and R. Huismans (2012), Low seismic velocities below mid-ocean ridges: Attenuation vs. melt retention, *J. Geophys. Res.*, *117*, B12403.
Goutorbe, B. (2010), Combining seismically derived temperature with heat flow and bathymetry to constrain the thermal structure of oceanic lithosphere, *Earth Planet Sci. Lett.*, *295*, 390-400.
Goutorbe, B., J. Poort, F. Lucazeau, and S. Raillard (2011), Global heat flow trends resolved from multiple geological and geophysical proxies, *Geophys. J. Int.*, *187*(3), 1405-1419.
Griffin, W. L., S. Y. O'Reilly, L. M. Natapov, and C. Ryan (2003), The evolution of lithospheric mantle beneath the Kalahari craton and its margins, *Lithos*, *71*, 215–241.
Grütter, H. S. (2009), Pyroxene xenocryst geotherms. Techniques and application. , *Lithos*, *112*, 1167–1178.
Hansen, L. N., C. Qi, and J. M. Warren (2016), Olivine anisotropy suggests Gutenberg discontinuity is not the base of the lithosphere, *Proc. Nat. Acad. Sci.*, *113*(38), 10503-10506.
Harrell, M. (2002), Anisotropic Lattice Thermal Diffusivity in Olivines and Pyroxenes to High Temperatures, 202 pp, Univ. Washington.
Harry, D. L., and W. P. Leeman (1995), Partial melting of melt metasomatized subcontinental mantle and the magma source potential of the lower lithosphere, *J. Geophys. Res.*, *100*(B7), 10255-10269.
Hasterok, D. (2013), A heat flow based cooling model for tectonic plates, *Earth Planet Sci. Lett.*, *361*, 34-43.
Hasterok, D., and D. S. Chapman (2007), Continental thermal isostasy: 1. Methods and sensitivity, *J. Geophys. Res.*, *112*, B06414.
Hasterok, D., and D. S. Chapman (2011), Heat production and geotherms for the continental lithosphere, *Earth Planet Sci. Lett.*, *307*, 59-70.
Hasterok, D., and M. Gard (2016), Utilizing thermal isostasy to estimate sub-lithospheric heat flow and anomalous crustal radioactivity, *Earth Planet Sci. Lett.*, *450*, 197-207.
Hasterok, D., and J. Webb (2017), On the radiogenic heat production of igneous rocks, *Geosci. Frontiers*, *8*(5), 919-940.
Hasterok, D., M. Gard, and J. Webb (2018), On the radiogenic heat production of metamorphic, igneous, and sedimentary rocks, *Geosci. Frontiers*, *9*(6), 1777-1794.
Hasterok, D., M. Gard, and M. Hand (2020), Controls on trace element chemistry and radiogenic heat production of volcanic arcs, *in prep.*
Hasterok, D., M. Gard, G. Cox, and M. Hand (2019), A 4 Ga record of granitic heat production: implications for geodynamic evolution and composition of the early Earth, *Precamb. Res.*, *331*, 105375.
Herron, M. M. (1988), Geochemical classification of terrigenous sands and shales from core or log data, *J. Sed. Res.*, *58*(5), 820-829.
Hillier, J. K., and A. B. Watts (2005), Relationship between depth and age in the North Pacific Ocean, *J. Geophys. Res.*, *110*, B02405.
Hirsch, A., C. A. Dalton, and J. Ritsema (2015), Constraints on shear velocity in the cratonic upper mantle from Rayleigh wave phase velocity, *Geochem. Geophys. Geosys.*, *16*, 3982–4005.

Höfer, M., and F. R. Schilling (2002), Heat transfer in quartz, orthoclase, and sanidine at elevated temperature., *Phys. Chem. Min.*, *29*, 571-584.
Hofmeister, A. M. (1999), Mantle values of thermal conductivity and the geotherm from phonon lifetimes, *Science*, *283*, 1699-1706.
Horai, K. (1971), Thermal conductivity of rock-forming minerals, *J. Geophys. Res.*, *76*, 1278-1308.
Horai, K., and G. Simmons (1969), Thermal conductivity of rock-forming minerals, *Earth Planet Sci. Lett.*, *6*(5), 359-368.
Huestis, S. P. (1984), Constraints imposed on crustal heat production by the linear heat flow relation, *Phys. Earth Planet. Int.*, *34*, 261-270.
James, D. E., F. R. Boyd, D. L. Schutt, D. R. Bell, and R. W. Carlson (2004), Xenolith constraints on seismic velocities in the upper mantle beneath South Africa., *Geochem. Geophys. Geosys.*, *5*(1), Q01002.
Jaupart, C., and J.-C. Mareschal (2007), Heat Flow and Thermal Structure of the Lithosphere, in *Treatise on Geophysics, Vol. 6*, edited by G. Schubert, pp. 217-251, Elsevier, Oxford.
Jaupart, C., and J.-C. Mareschal (2014), 4.2. Constraints on Crustal Heat Production from Heat Flow Data, in *Treatise on Geochemistry, Vol. 4, 2nd edition*, edited by R. L. Rudnick, pp. 53-73, Elsevier.
Jaupart, C., J.-C. Mareschal, and L. Larotsky (2016), Radiogenic heat production in the continental crust, *Lithos*, *262*, 398-427.
Jennings, S., D. Hasterok, and J. Payne (2019), A new compositionally-based thermal conductivity model for plutonic rocks, *Geophys. J. Int.*, *219*, 1377-1394.
Jones, A. G., J. C. Afonso, and J. Fullea (2017), Geochemical and geophysical constrains on the dynamic topography of the Southern African Plateau, *Geochem. Geophys. Geosys.*, *18*, 3556– 3575.
Karato, S.-i. (2012), On the origin of the asthenosphere, *Earth Planet Sci. Lett.*, *321-322*, 95-103.
Katz, R. F., M. Spiegelman, and C. H. Langmuir (2003), A new parameterization of hydrous mantle melting, *Geochem. Geophys. Geosys.*, *4*(9), 1073.
Kawakatsu, H., P. Kumar, Y. Takei, M. Shinohara, T. Kanazawa, E. Araki, and K. Suyehiro (2009), Seismic Evidence for Sharp Lithosphere-Asthenosphere Boundaries of Oceanic Plates, *Science*, *324*, 499-502.
Kelley, K. A., T. Plank, T. L. Grove, E. A. Stolper, S. Newman, and H. E. (2006), Mantle melting as a function of water content beneath back-arc basins, *J. Geophys. Res.*, *111*, B09208.
Kennedy, C. S., and G. C. Kennedy (1976), The equilibrium boundary between graphite and diamond, *J. Geophys. Res.*, *81*(14), 2467-2470.
Khan, A., A. Zunino, and F. Deschamps (2011), The thermo‐chemical and physical structure beneath the North American continent from Bayesian inversion of surface‐wave phase velocities. , *J. Geophys. Res.*, *116*(B9), B09304.
Khan, A., A. Zunino, and F. Deschamps (2013), Mantle thermochemical and anisotropic variations imaged beneath Australia from Bayesian inversion of surface-wave phase velocities, *J. Geophys. Res.*, *118*, 5285-5306.
Klöcking, M., N. J. White, J. Maclennan, D. McKenzie, and J. G. Fitton (2018), Quantitative Relationships between Basalt Geochemistry, Shear Wave Velocity, and Asthenospheric Temperature Beneath Western North America, *Geochem. Geophys. Geosys.*, *19*(9).
Korenaga, T., and J. Korenaga (2008), Subsidence of normal oceanic lithosphere, apparent thermal expansivity, and seafloor flattening *Earth Planet. Sci. Lett*, *268*, 41-51.
Lachenbruch, A. H. (1970), Crustal temperature and heat production: implications of the linear heat-flow relation., *J. Geophys. Res.*, *75*, 3291-3300.
Lee, C.-T. A., P. Luffi, T. Plank, H. Dalton, and W. P. Leeman (2009), Constraints on the depths and temperatures of basaltic magma generation on earth and other terrestrial planets using new thermobarometers for mafic magmas, *Earth Planet Sci. Lett.*, *279*(1), 20-33.

Leeman, W. P., D. L. Schutt, and S. S. Hughes (2009), Thermal structure beneath the Snake River Plain: Implications for the Yellowstone hotspot, *J. Volc. Geotherm. Res.*, *188*(1-3), 57-67.

Lévy, F., and C. Jaupart (2011), Temperature and rheological properties of the mantle beneath the North American craton from an analysis of heat flux and seismic data., *J. Geophys. Res.*, *116*, B01408.

Lucazeau, F. (2019), Analysis and mapping of an updated terrestrial heat flow dataset, *Geochem. Geophys. Geosys.*

Maggi, A., E. Debayle, K. Priestley, and B. G. (2006), Multimode surface waveform tomography of the Pacific Ocean: a closer look at the lithospheric cooling signature, *Geophys. J. Int.*, *166*, 1384–1397 doi: 1310.1111/j.1365-1246X.2006.03037.x.

Mareschal, J.-C., and C. Jaupart (2004), Variations of surface heat flow and lithospheric thermal structure beneath the North American craton, *Earth Planet Sci. Lett.*, *223*(1-2), 65-77.

Martos, Y. M., M. Catalán, T. A. Jordan, A. Golynsky, G. Eagles, and D. G. Vaughan (2017), Heat Flux Distribution of Antarctica Unveiled, *Geophys. Res. Lett.*, *44*, 11,417-411,426,.

Mason, B. (1952), *Principles of geochemistry*, John Wiley and Sons, New York.

Mather, B., L. Moresi, and P. Rayner (2019), Adjoint inversion of the thermal structure of Southeastern Australia, *Geophys. J. Int.*, *219*(3), 1648-1659.

Mather, K. A., D. G. Pearson, D. McKenzie, B. A. Kjarsgaard, and K. Priestley (2011), Constraints on the depth and thermal history of cratonic lithosphere from xenoliths, xenocrysts and seismology, *Lithos*, *125*, 729-742.

Matjuschkin, V., G. Brey, H. Höfer, and A. Woodland (2014), The influence of Fe3+ on garnet–orthopyroxene and garnet–olivine geothermometers, , *Contrib. Min. Pet.*, *167*(2), 972.

Maule, C. F., M. Purucker, N. Olsen, and K. Mosegaard (2005), Heat Flux Anomalies in Antarctica REvealed by Satellite Magnetic Data, *Science*, *309*(5733), 464-467.

McKenzie, D., J. Jackson, and K. Priestley (2005), Thermal structure of oceanic and continental lithosphere, *Earth Planet. Sci. Lett.*, *233*, 337-349.

McKenzie, D. P., and K. O'Nions (1991), Partial Melt Distributions from Inversion of Rare Earth Element Concentrations, *J. Petrol.*, *32*(5), 1021–1091.

McLaren, S., M. Sandiford, M. Hand, N. Neumann, L. Wyborn, and I. Bastrakova (2003), The hot southern continent: heat flow and heat production in Australian Proterozoic terranes, in *Evolution and dynamics of the Australian Plate*, edited by R. R. Hillis and R. D. Müller, Geol. Soc. Am. Spec. Pap. 372, Geol. Soc. Aus. Spec. Pub. 22.

Michaut, C., C. Jaupart, and D. R. Bell (2007), Transient geotherms in Archean continental lithosphere: New constraints on thickness and heat production of the subcontinental lithospheric mantle, *J. Geophys. Res.*, *112*, B04464.

Michaut, C., C. Jaupart, and J.-C. Mareschal (2009), Thermal evolution of cratonic roots, *Lithos*(109), 47-60.

Middlemost, E. A. K. (1994), Naming materials in magma/igneous rock system, *Earth Sci. Rev.*, *37*(3-4), 215-224.

Naif, S., K. Selway, and G. Egbert (2020), Electrical conductivity of the Lithosphere-Asthenosphere System, *Phys. Earth Planet. Int.*, *Special Issue Lithosphere-Asthenosphere*, in review.

Naif, S., K. Key, S. Constable, and R. L. Evans (2013), Melt-rich channel observed at the lithosphere–asthenosphere boundary, *Nature*, *495*, 356-359.

Nielson, S. (1987), Steady state heat flow in a random medium and the linear heat flow-heat production relationship, *Geophys. Res. Lett.*, *14*, 318-321.

Nimis, P., and W. R. Taylor (2000), Single clinopyroxene thermobarometery for garnet peridotites. Part 1, calibration and testing of a Cr-in-Cpx barometer and an enstatite-in-cpx thermometer. , *Contrib. Min. Pet.*, *139*, 541-554.

Nimis, P., and H. Grütter (2009), Internally consistent geothermometers for garnet peridotites and pyroxenites., *Contrib. Min. Pet.*, *159*, 411-427.

Nishimura, C. E., and D. W. Forsyth (1989), The anisotropic structure of the upper mantle in the Pacific, *Geophys. J. Int.*, *96*, 203-229.
O'Reilly, S. Y., and W. L. Griffin (2006), Imaging global chemical and thermal heterogeneity in the subcontinental lithospheric mantle with garnets and xenoliths: Geophysical implications, *Tectonophysics*, *416*, 289-309.
O'Reilly, S. Y., and W. L. Griffin (2010), The continental lithosphere-asthenosphere boundary: Can we sample it?, *Lithos*, *120*, 1-13.
O'Neill, H. S. C., and B. J. Wood (1979), An experimental study of Fe-Mg partitioning between garnet and olivine and its calibration as a geothermometer, *Contr. Mineral. and Petrol.*, *70*, 59.
Parsons, B., and J. G. Sclater (1977), An analysis of the variation of ocean floor bathymetry and heat flow with age, *J. Geophys. Res.*, *82*, 803–827.
Pasyanos, M. E. (2010), Lithospheric thickness modeled from long-period surface wave dispersion, *Tectonophysics*, *481*, 38-50.
Pasyanos, M. E., T. G. Masters, and G. Laske (2014), LITHO1.0: An updated crust and lithospheric model of the Earth, *J. Geophys. Res.*, *119*, 2153-2173.
Pearson, D. G., D. Canil, and S. B. Shirey (2003), Mantle samples included in volcanic rocks: Xenoliths and diamonds, in , vol. 2, The Mantle and Core, edited by , pp. , Elsevier, New York., in *The Mantle and Core*, edited by R. W. Carlson, H. D. Holland and K. K. Turekian, pp. 171–275, Elsevier, New York.
Perrin, A., S. Goes, J. Prytulak, D. R. Davies, C. Wilson, and S. Kramer (2016), Reconciling mantle wedge thermal structure with arc lava thermobarometric determinations in oceanic subduction zones, *Geochem. Geophys. Geosys.*, *17*.
Perry, H. K. C., C. Jaupart, J.-C. Mareschal, and N. M. Shapiro (2006), Upper mantle velocity-temperature conversion and composition determined from seismic refraction and heat flow, *J. Geophys. Res.*, *111*, B07301.
Petrunin, G. I., V. G. Popov, and I. A. Il'in (2004), Conductive heat transfer in plagioclases, *Izvestiya, Phys. Solid Earth*, *40*(9), 752-259.
Plank, T., and D. W. Forsyth (2016), Thermal structure and melting conditions in the mantle beneath the basin and range province from seismology and petrology, *Geochem. Geophys. Geosys.*, *17*, 1312-1338.
Pollack, H. N., and D. S. Chapman (1977), On the regional variation of heat flow, geotherms and lithospheric thickness, *Tectonophysics*, *38*, 279-296.
Pollack, H. N., S. J. Hurter, and J. R. Johnson (1993), Heat flow from the Earth's interior: Analysis of the global data set, *Rev. Geophys.*, *31*, 267-280.
Polyak, B. G., and Y. B. Smirnov (1968), Relationship between terrestrial heat flow and the tectonics of continents, *Geotectonics*, *4*, 205-213.
Priestley, K., and D. McKenzie (2006), The thermal structure of the lithosphere from shear wave velocities, *Earth Planet. Sci. Lett.*, *244*, 285-301.
Priestley, K., and D. McKenzie (2013), The relationship between shear wave velocity, temperature, attenuation and viscosity in the shallow part of the mantle, *Earth Planet Sci. Lett.*, *381*, 78-91.
Putirka, K. D. (2008), Thermometers and Barometers for Volcanic Systems, *Rev. Mineral. Geochem.*, *69*(1), 61-120.
Richards, F., M. Hoggard, A. Crosby, S. Ghelichkhan, and N. J. White (2020), Structure and dynamics of the oceanic lithosphere-asthenosphere, *Phys. Earth Planet. Int.*, *Special Issue Lithosphere-Asthenosphere*, in press.
Ritzwoller, M. H., N. M. Shapiro, and S.-J. Zhong (2004), Cooling history of the Pacific lithosphere, *Earth Planet. Sci. Lett.*, *226*, 69– 84.
Röhm, A. H. E., R. K. Snieder, S. Goes, and J. Trampert (2000), Thermal structure of continental upper mantle inferred from *S* wave velocity and surface heat flow, *Earth Planet Sci. Lett.*, *181*(395-407).
Roy, R. F., D. D. Blackwell, and F. Birch (1968), Heat generation of plutonic rocks and continental heat flow provinces, *Earth Planet Sci. Lett.*, *5*, 1-12.

Rudnick, R. L., and A. A. Nyblade (1999), The thickness and heat production of Archean lithosphere: Constraints from xenolith thermobarometry and surface heat flow, in *Mantle Petrology: Field Observations and High Pressure Experimentation: A Tribute to Francis R. (Joe) Boyd*, edited by C. M. B. Y. Fei and B. O. Mysen, pp. 3-12, The Geochemical Society.

Rudnick, R. L., and S. Gao (2003), Composition of the Continental Crust, in *Treatise on Geochemistry: The Crust*, edited by R. L. Rudnick, pp. 1-64, Elsevier.

Rudnick, R. L., W. F. McDonough, and R. J. O'Connell (1998), Thermal structure, thickness and composition of continental lithosphere, *Chem. Geol.*, *145*, 395-411.

Ruedas, T. (2017), Radioactive heat production of six geologically important nuclides, *Geochem. Geophys. Geosys.*, *18*(9), 3530-3541.

Ryan, C., W. L. Griffin, and N. Pearson (1996), Garnet geotherms: Pressure-temperature data from Cr-pyrope garnet xenocrysts in volcanic rocks, *J. Geophys. Res.*, *101*(B3), 5611-5625.

Rybach, L. (1988), Determination of heat production rate, in *Handbook of Terrestrial Heat Flow Density Determination*, edited by R. Haenel, L. Rybach and L. Stegena, pp. 125-142.

Rychert, C. A., and P. M. Shearer (2009), A global view of the lithosphere-asthenosphere boundary, *Science*, *324*, 495-498.

Sandiford, M., and S. McLaren (2002), Tectonic feedback and the orderign of heat producing elements within the continental lithosphere, *Earth Planet. Sci. Lett.*, *204*, 133-150.

Schatz, J. F., and G. Simmons (1972), Thermal conductivity of Earth materials at high temperatures, *J. Geophys. Res.*, *77*(35), 6966-6983.

Schutt, D. L., and C. E. Lesher (2006), Effects of melt depletion on the density and seismic velocity of garnet and spinel lherzolite, *J. Geophys. Res.*, *111*, B05401, doi: 05410.01029/02003JB002950.

Schutt, D. L., A. R. Lowrie, and J. S. Buehler (2018), Moho temperature and mobility of lower crust in teh western United States, *Geology*, *46*(3), 219-222.

Shapiro, N. M., and M. H. Ritzwoller (2004a), Thermodynamic constraints on seismic inversions, *Geophys. J. Int.*, *157*, 1175-1188.

Shapiro, N. M., and M. H. Ritzwoller (2004b), Inferring surface heat flux distributions guided by a global seismic model: particular application to Antarctica, *Earth Planet. Sci. Lett*, *223*, 213-224.

Sim, S. J., Spiegelman, M., Stegman, D., Wilson, C. (2020). The influence of spreading rate and permeability on melt focusing beneath mid ocean ridges. *Phys. Earth Planet. Int.* Special issue Lithosphere-Asthenosphere, in press.

Sleep, N. H. (2003), Survival of Archean cratonal lithosphere, *J. Geophys. Res.*, *108*(B6), 2302, doi:2310.1029/2001JB000169.

Smith, W. H., and D. T. Sandwell (1997), Global sea floor topography from satellite altimetry and ship depth soundings. , *Science*, *277*, 1956-1962.

Taylor, W. R. (1998), An experimental test of some geothermometer and geobarometer fomulations for upper mantle peridotites with application to the thermobarometery of fertile lherzolite and garnet websterite. , *Neues Jahrbuch fur Mineralogie- Abhandlungen*, *172*, 381–408.

Tesauro, M., M. K. Kaban, W. D. Mooney, and S. A. P. L. Cloetingh (2014), Density, temperature and composition of the North American lithosphere- New insights from a joint analysis of seismic, gravity, and mineral physics date: 2. Thermal and compositional model of the upper mantle, *Geochem. Geophys. Geosys.*, *15*, 4808-4830.

Turekian, K. K., and K. H. Wedepohl (1969), *Handbook of geochemistry*, Springer-Verlag, Berlin.

Van der Lee, S. (2002), High-resolution estimates of lithospheric thickness from Missouri to Massachusetts, USA, *Earth Planet Sci. Lett.*, *203*(1), 15-23.

Van Gerven, L., F. Deschamps, and R. D. Van der Hilst (2004), Geophysical evidence for chemical variations in the Australian continental mantle, *Geophys. Res. Lett.*, *31*, L17607, doi:17610.11029/12004GL020307.

Vilá, M., M. Fernández, and I. Jiménez-Munt (2010), Radiogenic heat production variability of some common lithological groups and its significance to lithospheric thermal modeling, *Tectonophysics*, *490*, 152-164.

Vosteen, H.-D., and R. Schellschmidt (2003), Influence of temperature on thermal conductivity, thermal capacity and thermal diffusivity for different types of rock, *Phys. Chem. Earth*, *28*, 499-509.

Wang, H., J. Van Hunen, D. G. Pearson, and M. B. Allen (2014), Craton stability and longevity: The rolse of composition-dependent rheology and buoyancy, *Earth Planet Sci. Lett.*, *391*, 224-233.

Yuan, H., and B. Romanowicz (2010), Lithospheric layering in the North American craton, *Nature*, *466*, 1063-1069.

Zlotnik, S. J., J. C. Afonso, P. Diez, and M. Fernández (2008), Small-scale gravitational instabilities under the oceans: Implications for the evolution of oceanic lithosphere and its expression in geophysical observables, *Phil. Mag.*, *88*(28), 3197-3217.

Zoth, G., and R. Hänel (1988), Appendix, in *Terrestrial Handbook of Heat-Flow Density Determination*, edited by R. Hänel, L. Rybach and L. Stegena, pp. 449-466, Kluwer.

Supplementary material for

Continental lithospheric temperatures: a review

Saskia Goes, Derrick Hasterok, Derek L Schutt, Marthe Klöcking

S1. Heat transfer equations

The basic equation for conductive heat transfer:

$$\frac{\partial T}{\partial t} = \nabla \cdot \kappa \nabla T - v \cdot \nabla T + A,$$

describes how temperature T varies with time t due to: heat conduction according to thermal diffusivity κ, heat advection according to material velocity v and internal heat production A. An additional source of heat can come from latent heat, most notably of melting. The heat flow, sometimes called heat flow or heat flow density, defines the heat loss - defined as a positive quantity - and is given by Fourier's Law,

$$q = k\nabla T,$$

where q is heat flow and k is thermal conductivity. The surface heat flow is simply defined as the vertical heat flow evaluated at a body's surface.

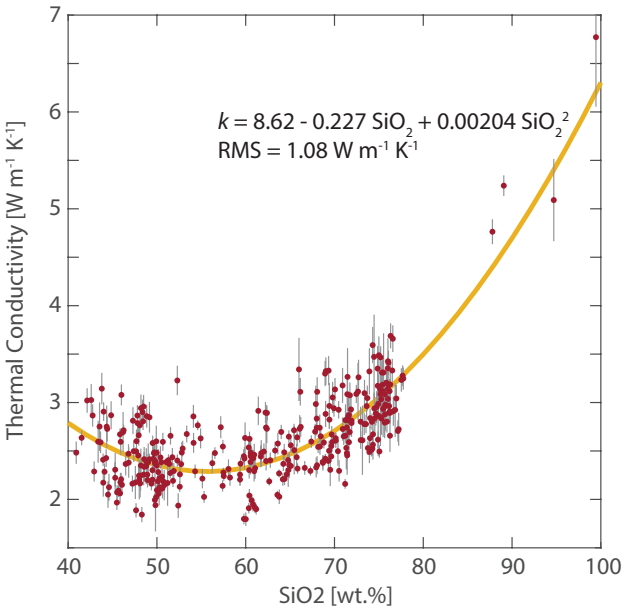

Fig. S1 – *Thermal conductivity variations with SiO_2 content. The data from Jennings (2017) include 331 plutonic, 9 low-porosity volcanic, and 4 quartzite samples.*

The thermal conductivity of silicate rocks is dominated by SiO_2 content. At standard temperature, there is a minimum in the average conductivity (2.3 W m^{-1} K^{-1}) at approximately 56 wt.% SiO_2, with felsic rocks generally having higher

conductivities than mafic rocks (Fig. S1). A simple quadratic conductivity model as a function of SiO_2 provides a good first-order approximation. The thermal conductivity can be modelled more accurately by taking into account additional oxides. [*Jennings et al.*, 2019] finds a misfit of only 0.28 W m^{-1} K^{-1} when using four major oxides. In Table 1 of the main text, we use the *Jennings et al.* [2019] model to estimate the thermal conductivity of a set of common rock types. The compositions are extracted from a global geochemical dataset [*Gard et al.*, 2019].

Macroscopic thermal conductivity of rocks can be anisotropic as a result of layering of compositions with differing conductivity (e.g., sandstones and shales, or quartzites and schists). Anisotropy also arises from the intrinsic anisotropy of some minerals (e.g., micas and olivine [*Gray and Uher*, 1977; *Xiong and Zhang*, 2019]) and their preferential alignment as a result of flow or tectonic stress. Anisotropy can also arise from the compositional layering resulting from deposition or cumulate formation during crystallization of plutons. Anisotropy is most important in foliated metamorphic rocks due to the alignment of highly anisotropic thermal conductivity of micas and sedimentary rocks with micro- and/or mesoscopic layering in shale and schist. Olivine is anisotropic, with $k_{[100]} > k_{[001]} > k_{[010]}$ [*Xiong and Zhang*, 2019], thus raising the possibility that mantle flow can result in enhanced heat flow in the direction of flow. However, the implications of thermal anisotropy within the mantle have not been fully explored. Perpendicular to bedding or foliation, the thermal conductivity of a package of sediments can be estimated by a weighted harmonic mean,

$$\bar{k}_h = \frac{1}{n}\sum_{i=1}^{n} k_i$$

and parallel to bedding or foliation, the thermal conductivity is best approximated by the weighted arithmetic mean, i.e.,

$$\bar{k}_a = \left[\frac{1}{n}\sum_{i=1}^{n} \frac{1}{k_i}\right]^{-1}$$

Table S1 - Physical properties of common rock types estimated from global geochemical compositions. Density model from Hasterok et al. (2018); Vp model from Behn and Kelemen (2003); heat production from Rybach (1988); and thermal conductivity from Jennings et al. (2019).

			SiO_2			density		P-wave velocity		thermal conductivity		heat production[b]											
												< 2 Ga						> 2 Ga					
			M[d]	min	max	μ	σ	μ	σ	μ	σ	*N*	μ	σ	μ_{ln}	σ_{ln}	M[d]	*N*	μ	σ	μ_{ln}	σ_{ln}	M[d]
Rock type[a]	**series**	***N***	**wt. %**			**kg m^{-3}**		**km s^{-1}**		**W m^{-1} K^{-1}**		**μW m^{-3}**											
								subalkaline															
quartzolite	plutonic	115	86.5	77.7	99.8	2708	58	5.99	0.14	4.19	0.37	28	1.53	1.08	0.11	0.98	1.11	2	0.51	0.15	-0.70	0.30	0.49
granite	plutonic	27192	73.9	69	86.7	2661	34	6.16	0.07	2.89	0.16	11681	3.27	3.91	0.91	0.75	2.48	2111	2.82	7.41	0.49	0.97	1.63
granodiorite	plutonic	9146	67.3	63	76.5	2722	36	6.40	0.09	2.68	0.12	4241	1.67	1.83	0.27	0.71	1.32	1000	1.05	1.65	-0.32	0.84	0.73
diorite	plutonic	3934	60.4	57	63	2795	43	6.65	0.11	2.47	0.10	2037	1.05	0.95	-0.19	0.71	0.83	238	0.71	0.56	-0.66	0.86	0.52
gabbroic diorite	plutonic	4743	53.8	52	57	2903	53	6.95	0.16	2.37	0.12	1951	0.67	1.98	-0.81	0.86	0.45	445	0.43	0.45	-1.14	0.80	0.32
subalkalic gabbro	plutonic	5471	50.3	45	52	2956	45	7.12	0.16	2.29	0.09	1974	0.33	0.45	-1.56	0.99	0.21	878	0.25	0.77	-1.91	0.98	0.15
peridotgabbro	plutonic	341	43.5	41	45	3034	80	7.42	0.25	2.14	0.10							47	0.27	0.47	-2.21	1.31	0.11
silexite	volcanic	306	88.1	77.8	99.4	2696	62	5.98	0.11	4.32	0.38							35	0.68	0.76	-1.14	1.38	0.32
rhyolite	volcanic	16695	74.8	69	87.1	2674	33	6.15	0.07	2.94	0.22	4705	3.17	7.14	0.92	0.67	2.51	758	1.49	1.09	0.18	0.66	1.20
dacite	volcanic	8576	66.5	63	77.2	2742	43	6.42	0.11	2.68	0.17	1859	1.50	1.06	0.17	0.76	1.18	570	1.03	0.69	-0.20	0.72	0.82
andesite	volcanic	10034	59.7	57	63	2813	45	6.68	0.12	2.47	0.10	2191	0.89	0.68	-0.35	0.72	0.70	583	0.85	1.23	-0.55	0.93	0.58
basaltic andesite	volcanic	17503	53.8	52	57	2900	44	6.93	0.13	2.36	0.10	3663	0.54	0.52	-0.93	0.81	0.39	1265	0.37	0.75	-1.55	1.01	0.21
subalkalic basalt	volcanic	21196	50.5	45	52	2958	33	7.12	0.11	2.30	0.08	3945	0.31	0.50	-1.55	0.89	0.21	1266	0.17	0.24	-2.09	0.72	0.12
picrobasalt	volcanic	264	43.9	41	45	3057	43	7.34	0.26	2.11	0.11	50	0.45	0.40	-1.20	0.94	0.30	15	0.51	0.55	-1.18	1.05	0.31
									alkaline														
quartz monzonite	plutonic	4355	66.4	61.2	71.1	2689	43	6.35	0.09	2.50	0.10	2219	2.72	2.97	0.78	0.63	2.19	305	2.36	5.88	0.32	0.81	1.38
syenite	plutonic	1356	62.7	57.7	71.1	2662	52	6.35	0.11	2.20	0.13	623	4.05	3.99	1.05	0.82	2.85	39	2.77	2.23	0.76	0.71	2.15
monzonite	plutonic	2809	58.6	53.2	63	2764	36	6.62	0.11	2.28	0.12	1380	2.14	2.98	0.45	0.73	1.58	146	1.26	1.18	-0.11	0.84	0.90
monzodiorite	plutonic	1933	53.5	49.5	57	2843	38	6.82	0.13	2.18	0.11	776	1.33	1.60	-0.04	0.80	0.96	100	0.98	1.07	-0.40	0.91	0.67
monzogabbro	plutonic	678	49.7	45.2	51.9	2907	34	6.96	0.13	2.09	0.08	271	1.07	4.14	-0.45	0.76	0.64	43	0.79	1.05	-0.65	0.90	0.52
alkalic gabbro	plutonic	1900	48.2	45	51.9	2951	41	7.05	0.12	2.13	0.07	753	0.46	0.58	-1.06	0.73	0.35	169	0.37	0.32	-1.31	0.85	0.27
trachydacite	volcanic	3720	66.1	61.2	70.9	2700	35	6.34	0.10	2.46	0.11	1098	2.51	2.01	0.74	0.59	2.09	77	1.84	1.17	0.40	0.68	1.49
trachyte	volcanic	2497	62.2	57.6	70.3	2672	35	6.33	0.09	2.13	0.12	625	4.88	4.87	1.29	0.74	3.62	6	1.94	1.22	0.54	0.52	1.71
trachyandesite	volcanic	5282	58.2	53.2	63	2769	33	6.62	0.12	2.25	0.13	1298	2.64	3.94	0.48	0.89	1.61	93	1.34	1.21	-0.05	0.87	0.95
basaltic trachyandesite	volcanic	6806	52.9	49.5	57	2847	31	6.83	0.12	2.15	0.10	1788	1.28	1.94	-0.07	0.74	0.93	112	0.70	0.47	-0.59	0.73	0.55
trachybasalt	volcanic	6028	49.0	45	52	2909	27	7.01	0.11	2.08	0.08	1540	0.97	0.94	-0.22	0.56	0.80	33	0.61	0.56	-0.77	0.77	0.46
alkalic basalt	volcanic	10023	48.0	45	52	2955	34	7.11	0.12	2.15	0.07	2922	0.61	0.68	-0.69	0.61	0.50	120	0.28	0.23	-1.52	0.70	0.22
									high-alkaline														
foid syenite	plutonic	405	57.1	52.5	62.7	2644	45	6.40	0.10	1.83	0.18							20	3.60	3.30	0.96	0.78	2.60
foid monzosyenite	plutonic	358	53.5	49.1	57.5	2758	42	6.73	0.14	2.08	0.18	243	3.79	1.63	1.23	0.47	3.43						
foid monzodiorite	plutonic	278	49.9	45.2	52.8	2825	47	6.94	0.15	1.98	0.14	133	3.76	3.52	1.08	0.68	2.95	3	1.35	0.67	0.20	0.60	1.22
foid gabbro	plutonic	517	44.8	41	49.1	2959	59	7.17	0.22	1.95	0.11	166	3.15	17.80	0.08	1.15	1.08	32	1.74	2.03	0.15	0.93	1.16
phonolite	volcanic	1037	58.1	52.5	62.8	2646	33	6.38	0.10	1.82	0.14	233	7.47	8.62	1.73	0.66	5.62						
tephriphonolite	volcanic	569	53.4	48.5	57.3	2746	39	6.69	0.14	1.95	0.15	144	4.60	3.60	1.28	0.70	3.58	1	9.54	0.00	2.26	0.00	9.54
phonotephrite	volcanic	997	49.5	45.1	53	2830	34	6.93	0.15	1.95	0.11	266	3.27	2.52	0.93	0.70	2.54	6	10.37	21.04	1.09	1.47	2.97
tephrite	volcanic	4278	44.7	41	49.3	2959	48	7.20	0.16	1.96	0.09	1039	1.44	1.88	0.16	0.57	1.18	15	0.75	0.44	-0.41	0.51	0.66
									high-magnesian														
mantle peridotite[e]	plutonic	1204	43.9	33.5	45	3323	35	8.13	0.11	3.17	0.22	98	0.13	0.38	-3.08	1.22	0.05	41	0.05	0.06	-3.45	0.96	0.03
mantle pyroxenite[e]	plutonic	79	43.5	33.5	45	3204	81	7.81	0.20	2.63	0.20	35	0.09	0.11	-2.90	1.08	0.06	6	0.09	0.07	-2.66	0.70	0.07
sanukitoid	volcanic	554	53.6	52	65	3012	96	7.35	0.26	2.84	0.34	62	0.23	0.45	-2.26	1.24	0.10	223	0.28	0.58	-1.97	1.18	0.14
gabbroic komatiite	volcanic	1460	46.5	45	52	3208	77	7.84	0.20	3.01	0.28	195	0.31	0.72	-2.14	1.39	0.12	183	0.14	0.18	-2.65	1.22	0.07
intrusive komatiite	volcanic	310	43.4	33.5	45	3246	62	7.82	0.19	2.69	0.20	142	0.19	0.66	-2.29	0.88	0.10	24	0.15	0.18	-2.45	1.07	0.09
boninite	plutonic	559	55.0	52	64.7	2944	73	7.13	0.21	2.67	0.25	72	0.19	0.33	-2.21	0.86	0.11	106	0.26	0.38	-2.07	1.23	0.13
meimechite	plutonic	1343	42.7	33	52	3218	86	7.92	0.35	2.50	0.21	324	1.86	1.53	-0.01	1.38	0.99	41	0.33	0.33	-1.39	0.74	0.25

basaltic komatiite	plutonic	1092	47.3	45	52	3152	55	7.69	0.15	2.80	0.18	86	0.26	0.70	-2.70	1.37	0.07	393	0.06	0.11	-3.39	0.95	0.03
komatiite	plutonic	342	43.1	33	45	3252	75	8.02	0.31	2.67	0.25	53	2.39	2.99	0.12	1.57	1.13	43	0.04	0.05	-3.61	0.81	0.03
ferropicrite	plutonic	723	45.3	33.1	52	3114	60	7.49	0.22	2.37	0.17	123	0.93	1.42	-0.87	1.35	0.42	136	0.22	0.19	-1.91	0.92	0.15
alkali ferropicrite	plutonic	418	42.1	33	51.6	3077	54	7.51	0.21	2.09	0.16	100	1.62	1.36	0.16	0.87	1.18	20	0.53	0.38	-0.77	0.47	0.46
picrite	plutonic	2847	48.1	33	52	3059	69	7.51	0.24	2.49	0.18	579	0.72	1.18	-1.34	1.52	0.26	288	0.17	0.38	-2.36	1.08	0.09
alkali picrite	plutonic	2798	45.2	33.2	52	3021	71	7.48	0.23	2.25	0.20	865	2.90	2.53	0.65	0.97	1.92	40	0.99	3.70	-1.10	1.13	0.33
									sedimentary														
														combined[c]									
quartzite		2231	89.2	72.5	99.8	2687.6	48					2231	1.74	4.69	-0.09	1.02	0.91						
quartz arenite		94	69.3	15.8	99.9	2959.8	212					94	0.62	2.58	-2.13	1.71	0.12						
litharenite		689	76.6	44.1	91.3	2734.1	58					689	2.50	4.46	0.57	0.68	1.76						
sublitharenite		86	75.5	44.8	97.2	2818.9	91					86	1.40	1.38	0.01	0.82	1.01						
arkose		1315	73.2	45.2	91.3	2683.8	74					1315	2.97	4.60	0.76	0.68	2.14						
subarkose		173	75.2	56.4	97.2	2765	91					173	2.25	5.34	0.17	0.84	1.18						
wacke		3859	70.5	38.1	85.8	2716.4	49					3859	2.71	4.44	0.72	0.60	2.06						
iron-rich sand		802	66.0	3	97.7	2896.7	154					802	2.79	7.72	0.06	1.27	1.06						
shale		4129	62.8	7.1	78.4	2749.4	45					4129	2.56	3.70	0.70	0.60	2.02						
iron-rich shale		2579	56.9	0.3	81.1	2861.1	84					2579	1.47	4.52	-0.15	0.83	0.86						
limestone		1554	29.8	0	57	2717.1	72					1554	1.48	5.17	-0.93	1.31	0.40						
dolomite		1227	32.3	0	61.9	2789	53					1227	1.69	6.30	-0.38	1.15	0.69						

[a]Plutonic rocks are estimated from total alkali-silica classification and IUGS high-magnesium classification (Middlemost, 1994) and sedimentary rocks are estimated using Sandclass (Herron, 1988).

[b]estimates < 2 Ga exlude Australian data between 2.0 and 1.4 Ga.

[c]sedimentary averages are independent of age

[d]median value

[e]the dataset used to train the thermal conductivity model is not calibrated to many ultramafics; lab experiments suggest the STP conductivity of ultramafics is higher than these estimated values.

Table S2 - Physical properties of estimated for common reference geochemical models. Density model from Hasterok et al. (2018); Vp model from Behn and Kelemen (2003); heat production from Rybach (1988); and thermal conductivity from Jennings et al. (2019).

			density		P-wave velocity		thermal conductivity		heat production	
			μ	σ	μ	σ	μ	σ	μ	σ
reference	layer	equivalent rock type	kg m^{-3}		km s^{-1}		W m^{-1} K^{-1}		μW m^{-3}	
Brodin (1998)	upper crust	granodiorite	2734		6.39		2.73			
Clarke (1889)	upper crust	diorite	2791		6.65		2.49			
Clarke and Washington (1924)	upper crust	monzonite	2772		6.60		2.40			
Condie (1993)	upper crust	granodiorite	2729		6.41		2.72		1.39	
Fahrig and Eade (1968), Eade and Fahrig (1973)	upper crust	granodiorite	2716		6.40		2.64		1.37	
Gao et al. (1998)	upper crust	granodiorite	2745		6.40		2.84		1.25	
Goldschmidt (1933)	upper crust	diorite	2763		6.48		2.60			
Ronov and Yaroshevskiy (1976)	upper crust	granodiorite	2753		6.47		2.70			
Rudnick and Gao (2003)	upper crust	granodiorite	2737	92	6.42	0.13	2.72	0.29	1.66	0.18
Shaw et al. (1967, 1976)	upper crust	granodiorite	2718		6.44		2.68		1.60	
Taylor and McLen (1985, 1995)	upper crust	granodiorite	2721		6.44		2.60		1.74	
Wedepohl (1995)	upper crust	granodiorite	2718		6.44		2.68		1.61	
Gao et al. (1998)	middle crust	granodiorite	2760		6.56		2.66		0.95	
Rudnick and Fountain (1995)	middle crust	diorite	2786		6.58		2.59		1.03	
Rudnick and Gao (2003)	middle crust	granodiorite	2773	92	6.57	0.13	2.63	0.29	0.99	0.12
Shaw et al. (1994)	middle crust	granodiorite	2684		6.31		2.77		0.93	
Weaver and Tarney (1984)	middle crust	granodiorite	2695		6.35		2.63		1.31	
Condie and Selverstone (1999)	lower crust	gabbroic diorite	2895		6.93		2.29		0.62	
Gao et al. (1998)	lower crust	diorite	2846		6.68		2.55		0.76	
Liu et al. (2001)	lower crust	diorite	2795		6.81		2.64		0.35	
Rudnick and Fountain (1995)	lower crust	gabbroic diorite	2900		7.01		2.43		0.20	
Rudnick and Gao (2003)	lower crust	gabbroic diorite	2900		7.01		2.42		0.20	
Rudnick and Presper (1990), updated	lower crust	gabbroic diorite	2917		7.06		2.37		0.13	
Rudnick and Taylor (1987)	lower crust	subalkalic gabbro	2985		7.14		2.43		0.12	
Shaw et al. (1994)	lower crust	diorite	2831		6.76		2.52		0.49	
Taylor and McLen (1985, 1995)	lower crust	gabbroic diorite	2909		6.92		2.42		0.35	
Villaseca et al. (1999)	lower crust	diorite	2760		6.41		2.62		0.80	
Weaver and Tamey (1984)	lower crust	diorite	2768		6.60		2.56		0.12	
Wedepohl (1995)	lower crust	diorite	2832		6.76		2.55		0.86	
Gale et al. (2013)	NMORB	subalkalic gabbro	2947	91	7.15	0.13	2.34	0.28	0.054	0.004
McDonough & Sun (1995)	NMORB	subalkalic gabbro	2950		7.18		2.32		0.04	
Workmann & Hart (EPSL, 2005)	mantle	mantle peridotite	3253		7.99		3.20		0.00	

S2. Non-steady state geotherms

Distributed stretching (or thickening) results in transient geotherms with similar monotonous shapes as the steady state geotherms. However, due to the disequilibrium between heat production and heat conduction, geotherm shape cannot be used to estimate heat production. For example, as lithospheric mantle cools after being thinned during rapid stretching, geotherm curvature can be similar to that expected from significant mantle heat production (Fig. S2).

On the other hand, if stretching or thickening is achieved by large scale faulting, initial geotherms could be strongly non-monotonous (Fig. S3). For thrust faulting this can lead to stacking of layers of different heat production, potentially with relatively high heat-production layers below lower heat production layers. Time scales for removing inverted thermal gradients that form by overthrusting are on the order the thickness of the layers involved (e.g., for crustal nappes of 10 km thickness, about 10 Myr), even if it takes up to thirty times longer to reach a full steady state (a time scale governed by lithospheric thickness), the deviations from steady state profiles may be difficult to observe on time scales more than 5-10 m.y. Even if the final configuration includes buried layers with high heat production similar to that of the upper crust, negative thermal gradients do not persist much longer and deviations from a smooth trend similar to those predicted by steady-state models are less than a few tens of degrees.

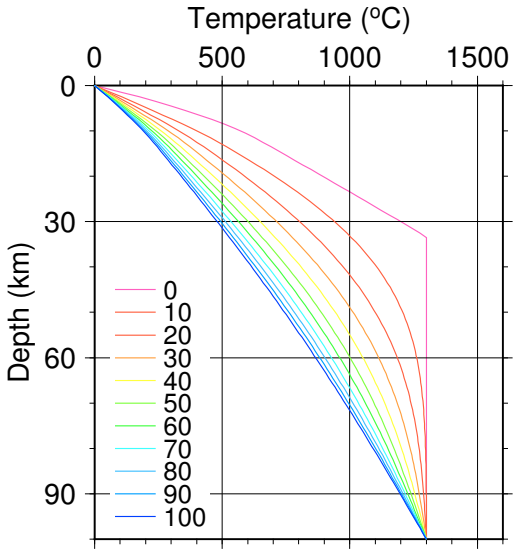

Fig. S2. *Example of geotherm evolution after instantaneous uniform stretching (by beta factor of 3) of initially 100 km thick lithosphere. Geotherms drawn every 10 m.y. Such models are commonly, and successfully, used to predict thermal basin evolution for hydrocarbon exploration.*

It has been noted before that the conductive heat flow expression of plumes that impinge at the base of thick lithosphere is expected to be minor [e.g. *Turcotte and Schubert*, 2002]. Indeed, if a 100-km thick lithosphere is exposed to a sudden source of heat from below (assuming this does not thin the thermal lithosphere), the effect on surface heat flow and Moho heat flow is small, less than 5 mW m^{-2} for a 300 degree basal temperature increase. By contrast, the effect on a thin lithosphere, e.g., 50 km thick, can be substantial, as large at 20 mW m^{-2}. This is of course away from areas where heat is advected by magma. In either case, removal of the pronounced

geotherm inflection takes no more than 10-20 Myr (longer for thicker lithosphere), although reaching full thermal equilibrium takes substantially longer (Fig. S4).

Even for locations with tectonic activity as recent as 10 to 20 Myr ago, steady-state profiles can be used to approximate thermal structure of the continental lithosphere, although the corresponding apparent heat production in mantle and crust could be significantly higher or lower than the actual heat production. Only with additional information of the evolution history, e.g., of topography, can the mechanisms responsible for the observed geotherm shape be deciphered.

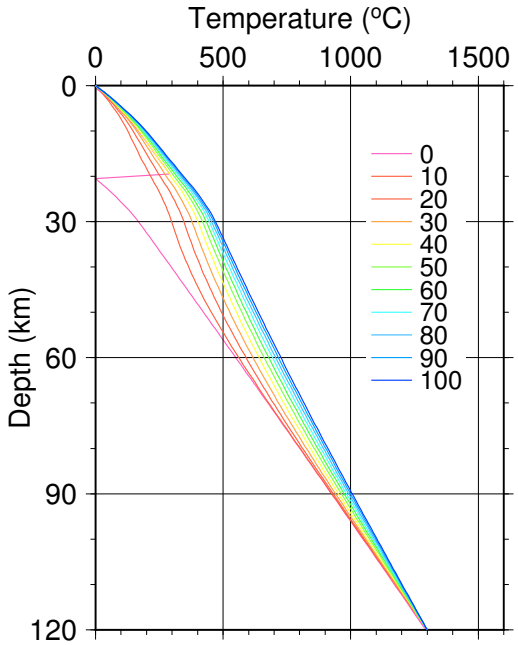

Fig. S3. *Example of geotherm evolution after instantaneous overthrusting a package of 10 km high-heat production (2 μW m^{-3}) crust plus 10 km mantle lithosphere of low heat production (0.02 μW m^{-3}) over a 10 km crust over 90 km mantle lithosphere with same heat production. Geotherms drawn every 5 m.y. Note that even for this end-member case, after only about 20 m.y. the negative thermal gradient from the overthrusting is hard to discern and deviations from a smooth shape similar to that of steady-state geotherms are at most a few tens of degrees.*

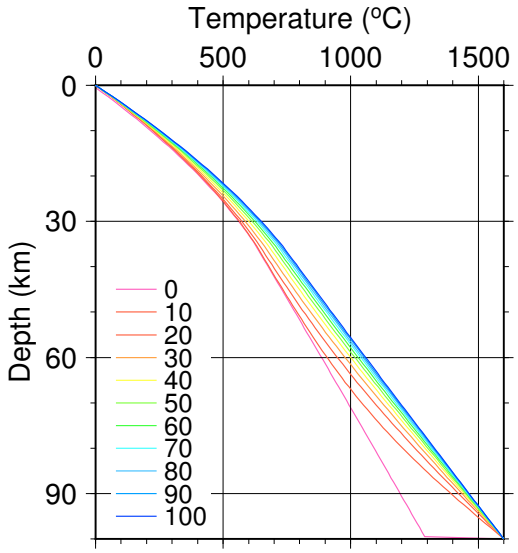

Fig. S4. *Example of geotherm evolution after imposing instantaneous heating (by 300°C) at the base of a 100 km thick lithosphere. The strong inflection at the base of the geotherms only persists for 10-20 Myr even for this thick lithosphere.*

References:

Gard, M., D. Hasterok, and J. Halpin (2019), Global whole-rock geochemical database compilation, *Earth System Sci. Data*, *11*, 1553–1566

Gray, A. S., and C. Uher (1977), Thermal conductivity of mica at low temperatures, *J. Mat. Sci.*, *12*, 959-965.

Jennings, S., D. Hasterok, and J. Payne (2019), A new compositionally-based thermal conductivity model for plutonic rocks, *Geophys. J. Int.*, *219*, 1377-1394.

Turcotte, D. L., and G. Schubert (2002), *Geodynamics*, Cambridge Univ. Press.

Xiong, Z., and B. Zhang (2019), Thermal transport properties of olivine, wadsleyite, and ringwoodite, *Minerals*, *9*, 519.